The Astrophysical Journal, 842:134 (25pp), 2017 June 20 https://doi.org/10.3847/1538-4357/aa755f

Pseudo-automatic Determination of Coronal Mass Ejections' Kinematics in 3D

Carlos Roberto Braga[1], Alisson Dal Lago[1], Ezequiel Echer[1], Guillermo Stenborg[2], and Rafael Rodrigues Souza de Mendonça[1]
[1] National Institute for Space Research—INPE, Av. dos Astronautas, 1758, São José dos Campos, SP, 12227-010, Brazil; carlos.braga@inpe.br
[2] Space Science Division, U.S. Naval Research Laboratory, 4555 Overlook Ave. SW Washington, DC 20375, USA
Received 2017 January 20; revised 2017 May 17; accepted 2017 May 22; published 2017 June 23

Abstract

Coronal mass ejection (CME) events are among the main drivers of geomagnetic disturbances, and hence play a central role in the Sun–Earth system. Their monitoring and, in particular, the determination of their speed and direction of propagation are key issues for the forecasting of space weather near to Earth. We have implemented a method to track CME events in three dimensions by combining triangulation and tie-pointing analysis with a supervised computer vision algorithm. This novel approach does not rely on any geometric constraint, and eliminates the need for visual identification of the CME boundaries. We applied our method to 17 CME events observed simultaneously by the twin *Solar Terrestrial Relations Observatory* (*STEREO*) COR2 coronagraph imagers from 2008 December to 2011 November in order to obtain their 3D kinematical characterization (i.e., the velocity vector) along with their morphological properties. About ten of these events have already been analyzed using other methodologies. In these cases, we carried out a thorough comparison with our results and found that, in spite of the different nature and spatial coverage range of the other methods with respect to CORSET3D, the majority of the results agree. We found, however, that three events exhibited discrepancies in the magnitude of the velocity vector, four in the longitudinal direction of propagation, and in only one case was there a discrepancy in latitude. The discrepancies appeared in those cases where quasi-simultaneous, quasi-co-located events were observed in the coronagraphs' fields of view.

Key words: interplanetary medium – solar–terrestrial relations – Sun: corona – Sun: coronal mass ejections (CMEs) – techniques: image processing

1. Introduction

Coronal mass ejection (CME) events play a central role in the Sun–Earth interaction because they are the main drivers of geomagnetic storms (Gosling 1990; Gonzalez et al. 1999; Schwenn et al. 2005). From an observational point of view, a CME is simply "an observable change in coronal structure that (1) occurs on a timescale between a few minutes and several hours, and (2) involves the appearance of a new, discrete, bright white-light feature in the coronagraph field of view (FOV)" (Howard et al. 1997). More recently, Mierla et al. (2010) described CME events as "enormous eruptions of magnetized plasma expelled from the Sun into interplanetary space, over the course of hours to days."

These dynamic structures have been studied for more than 40 years using observations from space-borne, white-light coronagraphs (Tousey 1973; Gosling et al. 1974). During solar minimum, approximately one event is observed every two or three days; at solar maximum, however, nearly five events per day can be observed (Howard et al. 1985; St Cyr et al. 2000; Gopalswany et al. 2001; Gopalswamy et al. 2015). These CME rates led to the observation of thousands of events in just one solar cycle (see, e.g., Wang & Colaninno 2014).

Generally, only about one out of ten CME events is geo-effective (see, e.g., Webb & Howard 1994; Gopalswamy et al. 2007; Webb & Howard 2012). Given the ever-increasing technological dependence of our society, it is therefore of crucial importance to improve the determination of both the direction of propagation and the kinematic properties of CMEs to gauge their potential time of arrival and geo-effectiveness. As seen on coronagraph images, some events show up as "halos" that either fully or at least to a great extent surround the occulting disk. Events exhibiting such morphologies are good candidates to trigger a geomagnetic storm. Gopalswamy et al. (2007) found that front-side CME halo events account for 11% of all CMEs observed by the LASCO coronagraphs (Brueckner et al. 1995) on board the *Solar and Heliospheric Observatory* (*SOHO*, Domingo et al. 1995), and that 70% of them are geo-effective. More recently, Shen et al. (2014) found that from all front-side CME halo events that were observed to fully cover the occulting disk (i.e., full-halo events) only 59% arrived at Earth. However, with coronagraph images from only a single viewpoint, it is difficult, if not impossible, to assess whether they develop toward or away from Earth.

Moreover, unlike limb events, the propagation speeds of halo CMEs (as projected onto the plane-of-sky) cannot be directly derived from a time series of coronagraph images due to projection effects (Schwenn et al. 2005). Therefore, some empirical methods have been developed to indirectly infer the propagation speed of halo CMEs (see, e.g., Gopalswamy et al. 2000; Dal Lago et al. 2003, 2013; Owens & Cargill 2004). However, the estimated arrival time at Earth obtained via any of the methodologies using only one viewpoint is still subject to significant uncertainties: the error is about ± 24 hr with a 95% error margin. More recently, Colaninno et al. (2013) investigated the performance of six methods to predict the arrival time of a set of nine events observed by the twin coronagraphs on board the *Solar Terrestrial Relations Observatory* (*STEREO*) S/C (Kaiser et al. 2008) and *SOHO*/LASCO. They found that the arrival time could be predicted with an error of ± 13 hr (full set considered), which is about half a day less than the error resulting from measurements from only one viewpoint.

Since the advent of the *STEREO* mission in 2006, the availability of cotemporal observations from two vantage points stimulated the development of techniques to infer the

three-dimensional aspect of CME events and hence facilitate the determination of their "true" kinematical and morphological properties. Briefly, the methodologies devised are based on the use of (1) forward modeling (see, e.g., Thernisien 2011a), or (2) triangulation, also called tie-pointing (see, e.g., Mierla et al. 2008 and references therein). These methodologies add up to other techniques that need only one viewpoint to infer the direction of propagation in 3D (e.g., techniques based on the properties of Thomson-scattered light; see Moran & Davila 2004). There are also methodologies based on the use of inverse methods, e.g., solar rotational tomography. These are beyond the scope of the paper, and will not be discussed here. For a detailed review of the different reconstruction techniques and their limitations and considerations, the reader is referred to Thernisien et al. (2011b).

The degree of polarization of Thomson-scattered light by coronal electrons is a function of the scattering angle between the direction of the incident light and the direction toward the observer (Billings 1966). By analyzing the ratio of polarized to unpolarized brightness, the scattering angle can be deduced and, therefore, the distance of the scattering location from the plane of the sky can be estimated using only one viewpoint (Moran & Davila 2004). The advantage of this method is that it does not need two viewpoints, and hence it could have been used before the *STEREO* era. However, this method does not disambiguate the direction of propagation, i.e., it cannot discern whether the event moves toward or away from the observer. More recently, this methodology was applied independently to the white light images from the coronagraph imagers on board both *STEREO* spacecraft and the results compared to each other (Moran et al. 2010). As shown by Mierla et al. (2009), the uncertainty in the direction of propagation inferred by this technique is larger than that resulting from methodologies based on two viewpoints.

Forward modeling techniques assume a physical and/or geometrical model of a CME. Thernisien et al. (2006) first proposed the graduated cylinder shell (GCS) model to represent the geometry of the CMEs observed by the LASCO C2 and C3 coronagraphs. The model consists of a tubular section attached to two cones that connect the main body of the CME to the solar surface. Later on, Thernisien et al. (2009) adapted the technique to simultaneously fit the model into the projection of the CME feature onto the plane of the sky of the FOV of the *STEREO* twin coronagraphs (COR1 and COR2; Howard et al. 2008). The methodology was later improved by incorporating a third viewpoint, i.e., the view from *SOHO*/LASCO, to better constrain the free parameters of the model. The geometrical model assumed for this methodology was that of a flux rope. However, many CMEs appear to develop with either distorted or asymmetric front shapes (e.g., Savani et al. 2010). Moreover, based on a statistical study, Vourlidas et al. (2013) showed that only about 40% of the CMEs observed exhibit the geometry of a flux rope. Therefore, the 3D morphology of many CME events cannot be properly represented by this approach.

Another set of methods requires the construction of elongation versus time plots (or J-maps; Sheeley et al. 1999) using information from a single viewpoint, extracted along a given position angle. The elongation is converted into position at distances higher than 30 solar radii by assuming that the CME speed and direction of propagation are constant from this point on. In these methods, a geometric model of the CME needs to be assumed. For instance, Rouillard et al. (2008) simply assumed radial propagation of a single plasma element along a straight line ("fixed Ø"), i.e., a model assuming point-like width. On the other hand, Lugaz et al. (2009) proposed the so-called harmonic mean method, which assumes that the CME is a radially expanding sphere anchored at the Sun (a quite wide structure in comparison to the point-like feature assumed in the fixed Ø method). Another approach is self-similar expansion fitting proposed by Davies et al. (2012), which allows more flexibility in the CME width than the other two methods cited above. In all these methodologies, the calculation of a central direction of propagation is strongly dependent on the assumption of the CME frontal geometry (Möstl et al. 2014).

Inhester (2006) introduced the concept of epipolar geometry and tie-pointing into the field of 3D reconstruction of CMEs. Given two images of the same scene from two different viewpoints, the tie-points refer to the pair of points (one on each image) that correspond to the projection of the same object (or feature) on each image. For an optically thin medium like that of the white light solar corona, the correspondence between pairs of points is not straightforward and frequently needs to be visually carried out. In epipolar geometry, the tie-points are constrained to a given straight line (called the epipolar line). Therefore, the matching of the tie-points becomes easier than achieving correspondence without any constraint (see, e.g., Mierla et al. 2008; Liewer et al. 2009, 2011; Feng et al. 2012).

To characterize the kinematical and morphological properties of the CME events as seen projected onto the plane of the sky of the coronagraphs in use, both manual and automatic methodologies have been proposed. As a result, catalogs abound in the literature, although they do not fully agree with each other. A manual, systematic study of thousands of CME events free from bias is a challenge mainly because of (1) the lack of a uniform and precise definition of a CME (which, in part, is influenced by the great variety of morphologies and shapes they exhibit), and (2) the subjective nature of the measurement process when performed by a human operator. A more extensive discussion about the importance of an objective characterization of CMEs can be found in Braga et al. (2013). Since the majority of the methodologies proposed so far might be influenced by decisions made from visual inspection, the problem becomes bigger when CMEs are studied in 3D.

For instance, in a catalog of CMEs such as the *SOHO* CDAW catalog[3] (Yashiro et al. 2004; Gopalswamy et al. 2009) an observer identifies the outermost point of the CME front in each frame simply by visual inspection. Due to the subjective nature of the process to select the outermost part of a CME front (sometimes not well defined), there are discrepancies when we compare such a catalog with other works that are also based on the visual identification of these fronts (e.g., St Cyr et al. 2000; Yashiro et al. 2004, 2008). Because of the data volume (e.g., *SOHO* alone spans over more than 20 years of continuous observations), the manual construction of a CME catalog is a very time-consuming task.

On the other hand, many techniques have been developed to track CMEs automatically. Their advantage with respect to manual methods is both the ability to handle large amounts of data, and the objectiveness (the detection of the CME features is based on a mathematical property, which is clearly defined in an algorithm). Among the different automatic CME catalogs in existence, we find the "Computed Aided CME Track" (CACTus)[4] catalog. This

[3] http://cdaw.gsfc.nasa.gov/CME_list/
[4] http://sidc.oma.be/cactus/

catalog is based upon an algorithm developed to detect automatically CME events on height–time maps of LASCO-C2, LASCO-C3, and SECCHI-COR2 images using the Hough transform (Robbrecht & Berghmans 2004; Robbrecht et al. 2009; Bonte et al. 2011). Another fully automated catalog is the "Solar Eruptive Event Detection System" catalog (SEEDS,[5] Olmedo et al. 2008), which is built upon an intensity-threshold-based algorithm running on LASCO-C2 images. Another catalog is the "Artemis Catalog of LASCO Coronal Mass Ejections" (Boursier et al. 2009), which is built using LASCO-C2 synoptic maps (see also Boursier et al. 2005). A second generation of this catalog, ARTEMIS II, is also available which, in addition to kinematic parameters, includes dynamic quantities such as mass and kinetic energy (Floyd et al. 2013). Another catalog available to the solar physics community is the coronal image processing (CORIMP[6]) CME catalog, which is built upon a methodology using dynamic signal separation and multi-scale edge detection (Morgan et al. 2012; Byrne et al. 2012; Byrne 2015). This catalog incorporates the so-called Automatic CME Triangulation method that allows automated detection of CMEs in three dimensions (Hutton & Morgan 2017).

A direct inter-comparison of the automated catalogs, as well as a comparison with the manual ones, will reveal discrepancies due to the different mathematical properties, image representations, and techniques used by the different catalogs to identify and track the CMEs (see Wang & Colaninno 2014). One drawback of CACTus, for example, is the splitting of some CMEs into two or more adjacent and simultaneous CMEs. Consequently, automatic catalogs tend to have a higher number of events recorded than manual catalogs do.

To avoid the limitation of methods that are either fully automatic or fully manual, Goussies et al. (2010) introduced a supervised computer vision algorithm to detect and track pseudo-automatically the CME events in the LASCO-C2 and -C3 FOVs (CORSET: Coronal Segmentation Technique). Braga et al. (2013) enhanced the capabilities of the CORSET algorithm by introducing new subroutines for the automatic determination of a more extended set of morphological and kinematical properties. And more recently, Vourlidas et al. (2017) used the CORSET algorithm to create the first dual, cross-linked CME catalog from *STEREO*/COR2.

In this work, we aim to develop a methodology to derive the velocity evolution (speed and 3D direction) of CME events (1) without using any geometric or physical assumption about the shape of the CME feature, and (2) without relying on manual determination of the CME boundaries. The technique devised combines CORSET with a triangulation-based methodology developed to reconstruct the CME fronts in three dimensions (Liewer et al. 2011). This novel approach will help answer questions such as: is the CME directed toward Earth? Does it develop above or below the ecliptic plane? Is it directed eastward or westward of the Earth? In other words, the state-of-the art methodology devised will help determine the CME real trajectory and kinematical properties, and hence it will contribute to reducing their estimated time of arrival at earth and to better assess their potential geo-effectiveness.

This paper is organized as follows: Section 2 describes the CORSET3D methodology, including (1) a brief review of the supervised algorithm to track the CME events (Section 2.1), (2) the 3D reconstruction approach (Section 2.2), (3) the derivation of the CME velocity (Section 2.3), and (4) a discussion on the error estimation (Section 2.4). The results are presented in Section 3, along with a brief discussion for each event analyzed to put them in context with previous works. In Section 4, we discuss the results from a global point of view. Finally, we present the conclusions in Section 5.

2. Method

We aim to determine the 3D velocity evolution of CME events that have been observed simultaneously by the COR2 instruments on board the twin *STEREO* S/C in a consistent manner. With such an objective in mind, we combined (1) a supervised computer vision algorithm for feature segmentation with (2) a triangulation technique constrained to epipolar geometry for the 3D reconstruction.

The *STEREO*/COR2 instrument is an externally occulted coronagraph (Howard et al. 2008). Its FOV extends from 2.5 to 15 solar radii at the nominal perihelion distance, the plate scale being 15 arcsec (2048 × 2048 pixels). The instrument is sensitive to photospheric light that is Thomson-scattered by free electrons in the corona (Billings 1966).

2.1. Pseudo-automatic Detection and Tracking of CME Events with a Supervised Computer Vision Algorithm in 2D

Goussies et al. (2010) introduced a texture-based, supervised methodology to detect and track CME events on a coronagraph FOV. CORSET is a supervised computer vision algorithm. It is not a manual method to identify the events because the CME boundaries are not identified by the user, nor is it a fully automatic method because there is still some user control and input (e.g., the user must define the time span of the event, delineate an initial guess of the CME boundaries in a given frame, and define in that frame a small region characteristic of the background).

Briefly, after the user-driven initialization stage, the CORSET algorithm detects and tracks the event as it develops in the user-specified sequence of images by analyzing the different textures of each image in the sequence. The sequence of images can be either raw or calibrated, although we used raw images in this study. The textures are computed by means of the Gray Level Co-occurrence Matrix (GLCM, Haralick et al. 1973). It is defined as a function of the spatial variation of the pixel intensities (gray levels). The elements of the GLCM are simply the relative frequencies of occurrence of pairs of gray-level values of pixels separated by a given distance in a certain direction. It is assumed that the texture information of an image is contained in the overall spatial relationship that the gray levels in the image have to one another. The GLCM captures and therefore characterizes the texture of the different regions. It is completely different on portions showing the CME, streamer, and background. On the other hand, it is similar on any portion of a given CME as seen on a given coronagraph image.

For each texture computed on each image, the algorithm performs a statistical test to decide whether it resembles the texture of the CME feature or of the background. The texture of the background is considered to be constant for all the images in the sequence, and it is computed in the small region defined by the user during the user-driven initialization stage. On the other hand, the texture that defines the CME is recomputed on

[5] http://spaceweather.gmu.edu/seeds/
[6] http://alshamess.ifa.hawaii.edu/CORIMP

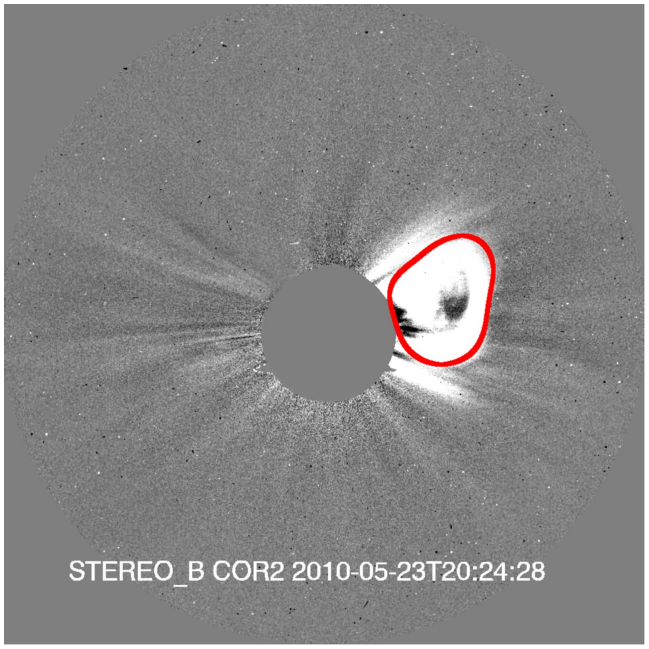

Figure 1. Example of a frame observed by *STEREO*/COR2 on board *STEREO B*. The red line delineates the region of the CME as identified by CORSET.

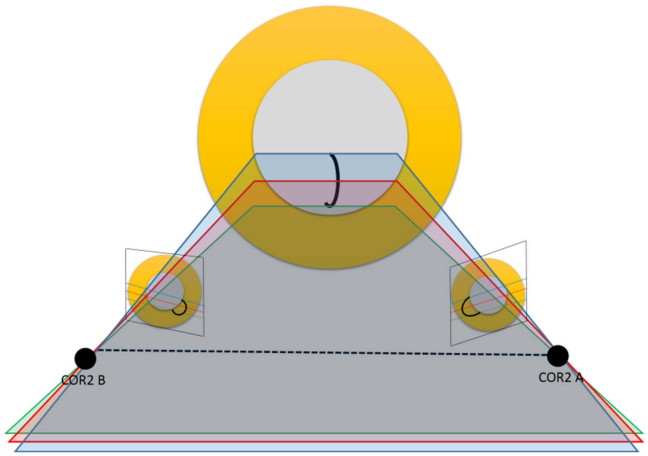

Figure 2. Illustration of the epipolar geometry used in the reconstruction of a loop line (represented by the black continuous line), which delineates the front of an ideal CME. The circle in gray represents the solar surface, and the yellow region illustrates the solar corona observed by the *STEREO*/COR2 coronagraphs (not to scale).

each new frame. This is necessary to account for potential changes in the texture of the CME along its evolution (e.g., to either include or exclude the presence of a shock in the segmentation). To achieve this, the algorithm requires upon initialization the setting of a user-defined parameter (the so-called expansion factor Q) that controls the degree of expansion of the CME area found in the preceding image. The area of the image used to compute the sample CME texture on the first frame is defined by the user. On the following frames, this area is an expansion of the area of the first frame. This expansion rate is adjusted by choosing the expansion factor. The reader is referred to Goussies et al. (2010) for examples, details, and the mathematical formulation of the procedure.

In Figure 1, we show an example of a CME feature observed by *STEREO*/COR2-B on 2010 May 23 at 20:24 UT.

Braga et al. (2013) extended the capabilities of the CORSET algorithm to allow the automatic determination of a wider set of morphological and kinematical properties of the tracked events (e.g., angular width, central position angle, radial speed, acceleration and expansion speed) and applied it to the study of 57 CME events observed by *SOHO*/LASCO. Concisely, they found that CORSET successfully detects and tracks the CME events if (1) they do not appear superposed by the coronagraph's pylon, and (2) there is no other CME partly superposed along its evolution. The radial speeds obtained were compared to those reported by the CACTUS and CDAW catalogs. The results obtained were within the 95% confidence limit for the majority of the CME events analyzed.

2.2. Three-dimensional Reconstruction of the CME Fronts Using Triangulation with Epipolar Geometry Constraint

In this work, the three-dimensional reconstruction of the CME front is done using triangulation of simultaneous observations of the event from two viewpoints. Epipolar geometry is used to better constrain the matching of the homologous locations (Inhester 2006). In Figure 2, we show a cartoon illustrating the use of epipolar geometry in the reconstruction of a loop line. In epipolar geometry, a plane (i.e., an epipolar plane) is defined by the location of the two observers and the particular feature (point) in the object. The line connecting the two viewpoints is called the stereo base line (black dashed line). For simplicity, only three epipolar planes are represented in Figure 2. For the reconstruction of the front of a CME event observed by a white light coronagraph as, e.g., *STEREO*/COR2, tens to hundreds of planes need to be defined.

Liewer et al. (2009, 2011) developed a tool (Sunloop) for the 3D reconstruction and visualization of white light features. The tool is available as part of the SECCHI IDL Solarsoft package and is based on the use of tie-points (triangulation). We incorporated part of the Sunloop methodology into CORSET to develop CORSET3D.

In CORSET3D, once a CME feature is segmented by CORSET in the two simultaneous images obtained by the two *STEREO*/COR2 instruments, the image pair is rotated so that the rows become parallel to the stereo base line (in this new configuration, the epipolar lines become horizontal). Due to the epipolar constraint, any given point of the CME front lies in the same epipolar line in both images. Therefore, once a point is fixed in one viewpoint, the matching point on the other viewpoint is restricted to be selected only along one dimension of the image. These pairs of points, one on each image, are called tie-points. The 3D location of the tie-pointed feature is the intersection of the two camera rays.

CORSET3D benefits from both the feature segmentation capabilities offered by CORSET and the 3D reconstruction approach used by Sunloop. Therefore, it allows the automatic 3D reconstruction of CME fronts of any shape (neither CORSET nor Sunloop imposes a geometric configuration or shape). In particular, the CME contour obtained by CORSET is used as input for the reconstruction "as it is," i.e., without any change. Since we assume that the CME boundaries obtained by CORSET correspond to the same physical structure on both simultaneous *STEREO*/COR2 images, we consider that the tie-points are

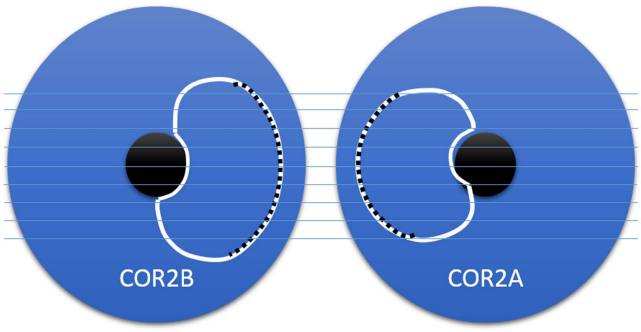

Figure 3. Determination of tie-points along the CME front (white contour) on a pair of coronagraph images. The blue area represents the *STEREO*/COR2 fields of view. The blue horizontal segments delineate the epipolar lines. The tie-points are automatically defined by CORSET3D on the region indicated by the dashed black curve.

defined by the intersection of the outermost portion of the CME contour with the epipolar lines (see Figure 3).

Unlike the original version of the "Sunloop" tool, where the user has to define manually the tie-points on each pair of images, CORSET3D allows for the automatic determination of the tie-points all along the leading edge of the event in every pair of images where the CME was detected. Typically, the CORSET3D algorithm defines from 50 to 200 tie-points on each *STEREO*/COR2 image, depending on factors such as shape, irregularity, and length of the contour line that defines the CME front. After the tie-pointing is completed for all the images in the user-defined sequence where the CME is visible, the points obtained by triangulation are connected with straight-line segments to help visualize the portion of the CME front to be reconstructed. We observed that the tie-points close to the lateral side of the CME produce inconsistent results, probably because they do not point to the same CME feature in both viewpoints. For this reason, for reconstruction purposes we restricted the angular range and ignored the points of the contour on the flanks of the CME (see the black dashed line in Figure 3).

Once the set of tie-point pairs for a given segmented CME front is defined, Sunloop is used to perform the triangulation following the procedure described in Liewer et al. (2011). The upper panel of Figure 4 shows an example of the CME front reconstruction and its 3D evolution using Sunloop as part of CORSET3D (automatic determination of the tie-points). For comparison, the 3D reconstruction and evolution of the same front using Sunloop in its original form (manual selection of tie-points) is shown in the bottom panel of the figure. We note on the 3D view exhibited in the right panels of the figure the more consistent and smoother shape of the CORSET3D reconstructed fronts. This is typical for any event analyzed in this work. As the CORSET3D reconstruction involves a substantial part of the CME's leading edge (which is defined in an objective way), more comprehensive studies are possible.

2.3. Determination of the CME Front Velocity

Each pair of tie-points determines a reconstructed CME front point (hereafter FP) in three-dimensional space. As the linear separation between each set of tie-points determined by the algorithm is kept constant along the development of the event, the number of FPs will increase with the radial distance of the event from the Sun. Likewise, the wider the CME, the more FPs there will be.

Since we are interested in the CME 3D propagation, it is necessary to follow the individual FPs in time. The FPs are not exactly radially aligned in consecutive time instances. Moreover, the total angular span covered by the FPs might be different along the front's evolution. Therefore, we first need to group the FPs in angular ranges, i.e., we split the latitudinal and longitudinal angular spans in o and p steps of one degree, respectively, and define radial directions combining any possible longitude and latitude inside this range in steps of one degree. Then, for a given radial direction (θ_j, ϕ_k) at each time instance i, we find the closest FP to the given radial line and determine its distance to the Sun. If the distance from the FP to the radial direction is too large (i.e., higher than the limit of 300,000 km we ad hoc imposed) we ignore this point. The limit chosen corresponds to approximately an angular difference of 3° at 10 solar radii. We call the radial directions corresponding to the ignored points "ignored radial directions" (hereafter IRDs). In this way, we have defined a set of points $P(t_i, \theta_j, \phi_k)$ that represents the location of the CME front at each time instance i (t_i represents the time instance, and θ_j and ϕ_k denote the latitude and longitude, respectively, that define a radial direction).

The 3D time evolution of the CME front is characterized by the points $P(t_i, \theta_j, \phi_k)$. Therefore, the instantaneous propagation speed v_r in the radial direction specified by the angles (θ_j, ϕ_k) can be computed using the following expression:

$$v_r(t_i, \theta_j, \phi_k) = \frac{P(t_i, \theta_j, \phi_k) - P(t_{i-1}, \theta_j, \phi_k)}{t_i - t_{i-1}} \quad \begin{matrix} i = 2, ..., n \\ j = 1, ..., o \\ k = 1, ..., p. \end{matrix} \qquad (1)$$

In addition, we calculate the time average of the radial speed $\overline{v_r}$ for each direction (θ_j, ϕ_k) by fitting a straight line to the points $P(t_i, \theta_j, \phi_k)$. The number of points used for each fit corresponds to the number of time instances available. Figure 5 shows an example of a height–time plot used to compute the average speed at a particular radial direction, $(\theta_j, \phi_k) = (-2°, 5°)$, for a CME event on 2010 May 23.

Given the latitudinal and longitudinal span of a CME front in o and p steps of one degree, $\overline{v_r}$ is calculated $o \cdot p$ times, typically from tens to hundreds of times, depending of the angular span of the CME FPs. As mentioned above, $P(r_i, \theta_j, \phi_k)$ and the corresponding $\overline{v_r}$ are discarded for the IRDs. The resulting set of directions (i.e., $o \cdot p$ minus the number of cases ignored) is called accepted radial directions (hereafter ARDs) and its number (typically in the range of tens) is hereafter referred as NARD.

For illustration purposes, we represent $\overline{v_r}$ over a spherical shell representing the portion of the solar corona that faces an observer sitting at Earth. Each $\overline{v_r}$ is represented by a square located in the appropriate direction (latitude and longitude). An example of such a representation for a CME event observed on 2010 May 23 is shown in Figure 6. The color of each square represents the corresponding speed. Note that the diameter of the square representing each radial velocity was chosen only for convenient visualization purposes and does not represent any physical parameter. The radial direction whose latitude and longitude are the midpoints of their ranges is indicated by a black diamond. The time span used to calculate $\overline{v_r}$ is indicated below the color bar.

The representation chosen to plot the radial velocities of a given event allows us to discern the speed evolution of the CME front. In the example shown in Figure 6, it is clearly

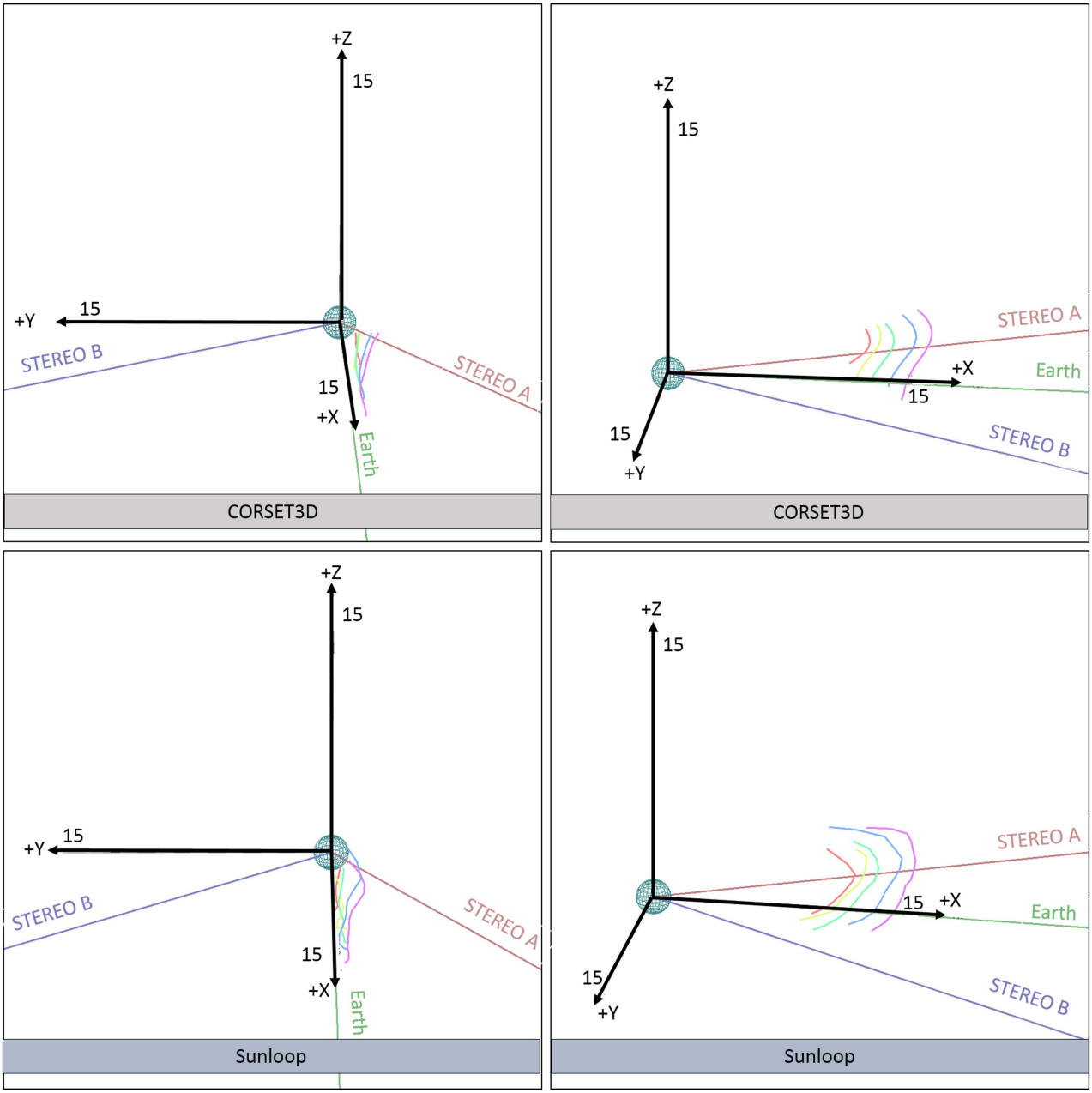

Figure 4. 3D reconstruction and evolution of a CME event's front observed on 2008 December 12. Upper panel: CME fronts reconstructed using CORSET3D. The front was reconstructed at five different time instances (each one is represented by a line with a different color). Bottom panel: corresponding CME fronts reconstructed using Sunloop in its original form. On the left panels, the observation point is close to the Sun–Earth line (represented in green) and on the right panels the observation point is almost perpendicular to this line. The axis units are given in solar radii.

shown that the average speed tends to be higher in the northernmost portion of the CME front. This information is intended to be used in future analyses as an indicator of the difference in the magnitude of the forces applied to the CME in the solar corona at different portions of its latitudinal and/or longitudinal extension. It can also be noted in the figure that the front of the CME is inclined with respect to the meridians. This inclination is likely to be related to the large tilt angle of the CME with respect to the ecliptic, which can be derived from the GCS model (as discussed in Lugaz et al. 2012).

For comparison purposes, we also compute the average velocity vector $\langle V \rangle$ using all values of $\overline{v_r}(\theta_j, \phi_k)$ available for a given CME event. Each orthogonal component of $\langle V \rangle$ corresponds to the mean value of the corresponding orthogonal components of $\overline{v_r}(\theta_j, \phi_k)$. The velocity vector $\langle V \rangle$ calculated in this way is then converted back to spherical coordinates in order to express the speed, latitude, and longitude of the CME propagation.

The results from CORSET3D are reported in the Stonyhurst coordinate system. This system is derived from the Heliocentric Earth Equatorial (HEEQ) coordinate system, where x is the intersection between the solar equator and central meridian as seen from the Earth, and z is directed toward the north pole of the solar rotation axis (Hapgood 1992). The coordinates resulting from the conversion of the HEEQ coordinate system into spherical coordinates are frequently called Stonyhurst heliographic coordinates (Thompson 2006). The angles θ and ϕ are given in degrees with θ increasing toward solar north and ϕ

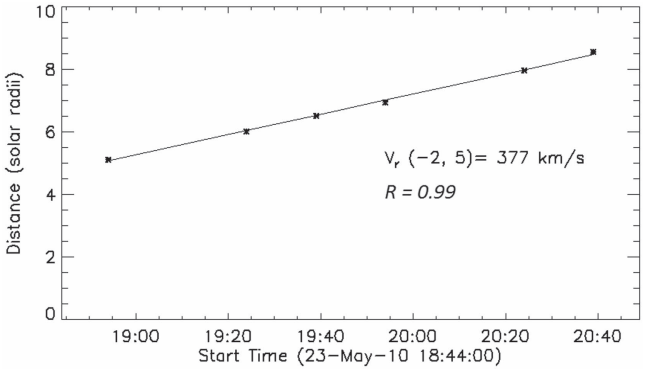

Figure 5. Height–time plot at a sample direction $(\theta_j, \phi_k) = (-2°, 5°)$ for the CME event observed by the twin *STEREO*/COR2 coronagraphs on 2010 May 23. The line indicates the best fit to the data points (represented by asterisks) used to estimate the radial speed V_r. The linear Pearson correlation coefficient R is also indicated.

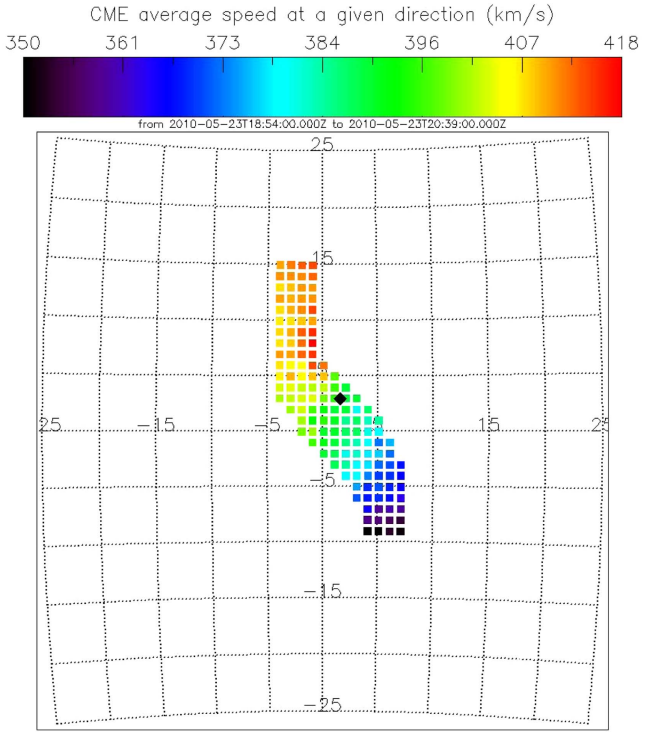

Figure 6. Linear radial speed $\overline{v_r}$ of the CME front observed by the twin *STEREO*/COR2 coronagraphs on 2010 May 23 as a function of latitude and longitude (in the Stonyhurst coordinate system). The black diamond indicates the radial direction whose latitude and longitude are the midpoints of their ranges.

increasing toward the west limb of the Sun. Some results from previous works discussed in this paper are given in Heliocentric Earth Ecliptic (HEE) with x pointing from the Sun to the Earth and z toward ecliptic north pole. The remaining axis completes the right-handed Cartesian triad and points approximately toward the west limb. Notice that the difference between the HEE and HEEQ is the inclination of approximately 7° between the solar equatorial and the ecliptic planes.

2.4. On the Estimation of Errors in the 3D Reconstruction of the CME Front Velocity

The error in the determination of the individual tie-points on each image is due to (1) the finite resolution of the image, and (2) the intrinsic error of the methodology employed to obtain the CME front. On the other hand, and as shown in Mierla et al. (2010), the error on the resulting 3D point reconstructed on a given epipolar plane is $ds/\sin(\gamma/2)$, where γ is the separation angle between the two *STEREO* spacecraft, and ds is the pointing error on each image along the corresponding epipolar line. For example, the S/C separation on the date of the event shown in Figure 6 (i.e., 2010 May 23) is $\gamma = 142°$, and hence the error is about 1.06 ds. Likewise, since γ was 87° on the date of the event depicted in Figure 4 (i.e., 2008 December 12), the corresponding error is 1.46 ds. (The larger the separation angle, the smaller the error.)

Another source of error that is uniquely related to the tie-point based triangulation technique is due to the optically thin nature of the white-light corona. As a result of this, a CME front stems from the line-of-sight integration, and hence each coronagraph may see different apparent leading edges depending upon the separation angle between the instruments. Liewer et al. (2011) termed this the "different-apparent-leading-edge" (DALE) effect. For this work, we calculated an estimate of this error using the model proposed by Liewer et al. (2011) under the following assumptions.

(1) The CME is located on the ecliptic plane and the longitude β of the propagation angle (as measured at the central part of the CME) is close to the Sun–Earth line. The majority of the events studied in this work have $\beta < 20°$.
(2) Both *STEREO* spacecraft are located at a distance of approximately 1 au from the Sun and at a similar angular distance θ from the Sun–Earth line but on different sides. For the events analyzed in this work, $40° < \theta < 105°$.
(3) The CME can be modeled by a spherical shell with radius a and with its center at a distance R from the Sun. Since the geometric shape of a spherical shell is under-constrained to what we defined as the apex of the CME front extracted from CORSET, there is no direct way to extract a/R from CORSET3D. Therefore, in order to illustrate how the errors are related to the a/R ratio, we adopt the same two arbitrary values adopted by Liewer et al. (2011), i.e., $a/R = 0.5$ and $a/R = 1$.
(4) The brightest features in the coronagraph will result from lines of sight with the longest path length through the CME.
(5) The coronagraphs can be interpreted as cameras at infinite distance from the solar corona so that the camera rays can be considered parallel. This assumption is reasonable because when a CME is in the coronagraph FOV, the distance from the Sun is a few solar radii and the distance to the spacecraft is much higher (about 200 solar radii).

Under these assumptions, the trend is that the speeds derived by CORSET3D are always higher than the speed of the CME if no DALE effect exists. This error decreases as the separation angle between each spacecraft and the Sun–Earth line increases. On the other hand, it increases proportionally with the ratio a/R. At the beginning of the CME period analyzed here (2008 December) the error is up to 20% if $a/R = 0.5$, and up to 30% if $a/R = 1.0$. For the events in 2011, the error is lower than 5%. There is no significant difference in the speed error as β increases.

The estimated longitudes tend to be smaller than the longitude if no DALE effect exists and they increase with β. The highest error found under the assumptions described above

is 12°, which occurs when $a/R = 1$, $\beta = 20°$, and the separation angle between the two spacecraft is minimum ($\theta = 40°$). On the other hand, if $\beta = 10°$, the maximum error is 6°.

This brief discussion shows that the track of CMEs developing at greater angular distances from the Sun–Earth direction, i.e., those events exhibiting a greater β, are subject to larger errors, and hence it imposes a limitation on the reliability of CORSET3D for these particular events.

3. Results

We selected all the CME events between 2008 and 2011 likely associated to interplanetary coronal mass ejections (ICMEs) in the interplanetary medium around Earth that exhibited signatures of magnetic clouds (MCs) according to the catalog of Richardson & Cane (2010).[7] Note that we chose from that list only those events marked as "MC2." We did not include in the analysis ICME events that lacked evidence of rotation in the magnetic field direction and/or enhanced magnetic field (indicated as "MC1" and "MC0" in the Richardson and Cane list).

We used CORSET3D (1) to detect and track the selected events during the early stages of their evolution in the FOV of the *STEREO*/COR2-A and /COR2-B coronagraphs, and (2) to compute both their direction of propagation in 3D space (latitude and longitude) and mean vector velocity. The twin *STEREO* spacecraft are located approximately at 1 au from the Sun, one ahead of the Earth and one behind it in its orbit around the Sun. The S/C separation ranged between ∼80° and ∼210° during the time period of interest, the Sun–Earth line being approximately at the mid-angular distance between both S/C.

From the list of MCs marked as MC2 reported in the Richardson and Cane catalog, we identified the likely associated CMEs. For some MCs, more than one CME event were likely to be the solar counterpart. In those few cases, all the probable associated CMEs were analyzed here, with the exception of those cases that needed to be removed from the analysis due to limitations on the methodology. For instance, in one case (2010 February 7), the results from CORSET were discarded because the segmented area was not consistent with the CME definition. For two other CMEs (which were associated with the MCs observed on 2010 December 28 and 2011 February 4), the triangulation could not be performed because the separation of the *STEREO* spacecraft was close to 180°. For a few other MCs in the catalog (on 2009 February 3, 2011 May 28, and 2011 November 7), we could not identify any CMEs directed toward the Earth in the *STEREO* coronagraphs. For the remaining MCs in the catalog, we identified and tracked the Earth-directed CMEs.

Table 1 summarizes the list of events analyzed in this work, along with the S/C separation at the time of each event, the parameters used by CORSET3D for the tracking, the results, and a categorical comparison with previous works. The first row shows the CME event identification number and the date of observation. The separation between the *STEREO* spacecraft for each event is indicated in the second row. The observation time (UT) of the first and last frame used by CORSET3D for the CME tracking is indicated in the third and fourth rows, respectively. The total number of usable frames in the time sequence used to track each event in both coronagraphs is specified in the fifth row. The sixth row shows the user-defined expansion parameter adopted to track the corresponding event on *STEREO A* and B, respectively (see details in Section 2.1).

The seventh row indicates the computed de-projected heliocentric distance of the CME front at the time of the first and last frames. The next row indicates the estimated error on the triangulation as derived from the Sunloop method (i.e., the distance of closest approach between the two lines of sight). The ninth row indicates whether we identified other CME event in the FOV of the coronagraphs during the time period of the corresponding CME (close in position angle).

Table 1 also includes the computed average velocity vector $\overline{v_r}(\theta_j, \phi_k)$ (i.e., the speed magnitude and direction, as defined in Section 2.3, including the NARDs), along with the minimum and maximum values computed for any given CME front. The latitudinal (θ_1, θ_o) and longitudinal ranges (ϕ_1, ϕ_p) used to calculate $\overline{v_r}(\theta_j, \phi_k)$ are also indicated in the table.

In the following subsections, we briefly compare the results derived from CORSET3D with previous works using other techniques that relay on two viewpoints. We also elaborate on the plausible reasons for the discrepancies. For some of the events observed during 2011 (i.e., events #13, #14, #15 and #17) we did not find previous references using simultaneous observation from two viewpoints, and hence we do not discuss them in detail.

3.1. Event #1: CME Event on 2008 December 12

The CORSET3D segmentation of the CME event observed on 2008 December 12 by the twin *STEREO* COR2 coronagraphs is shown in Figure 7. The leading edge of the CME obtained by our algorithm is consistent all along the time sequence. Note that the segmentation of the event failed in the inner portion of *STEREO* COR2A images (top panel), which presents no hindrance for the purposes pursued in this work. This undesired effect is due to a bad selection of the base image (there is a bright structure in the base image chosen, hence the dark region close to the limb). Since the determination of the velocity vector is not affected by this issue we chose to keep this base image for illustration purposes and to help explain the caveats of the algorithm (compare it to the segmentation obtained for COR2B).

Earlier stages of the CME development in the FOV of the COR2 instruments are not shown in Figure 7. At these earlier time instances, CORSET was able to segment the CME; however, these results had to be ignored because they led to NARD equal to zero on the application of CORSET3D.

The radial speeds derived by CORSET3D as a function of latitude and longitude are shown in Figure 8. The CORSET3D reconstruction shows that this CME event propagates in the inner portion of northwest quadrant of the solar corona (as seen from Earth, see Figure 8) up to at least a heliocentric distance of 16 solar radii (de-projected distance by the time the event reached the end of the time period selected, i.e., 13:37 UT). Figure 8 indicates that the radial speed is lowest at the northernmost portion of the reconstructed CME front. Further analysis is necessary to assess whether the speed differences along the front are artifacts resulting from the segmentation or a true effect. Byrne et al. (2010) also studied this event using a technique based on triangulation and found a speed of about 400 km s^{-1} between 10 and 15 solar radii. Using the GCS model, Möstl et al. (2014) found that the initial speed of this CME was about 497 km s^{-1}.

[7] http://www.srl.caltech.edu/ACE/ASC/DATA/level3/icmetable2.htm

Table 1
List of Events Analyzed Including the Tracking Parameters and Main Results Derived using CORSET3D

CME # and Date/Parameters		#1 2008 Dec 12	#2 2010 Apr 3	#3 2010 Apr 8	#4 2010 May 23	#5 2010 May 24	#6 2010 Aug 1	#7 2010 Aug 1	#8 2011 Mar 25	#9 2011 Sep 6	#10 2011 Sep 6	#11 2011 Sep 7	#12 2011 Sep 9	#13 2011 Sep 14	#14 2011 Oct 1	#15 2011 Oct 2	#16 2011 Oct 22	#17 2011 Nov 26
Spacecraft separation angle (degrees)		86.7	138.6	138.9	141.5	141.6	149.6	149.6	176.1	162.3	162.3	162.1	161.8	161.0	158.2	158.1	154.6	148.2
Tracking parameters	First frame time	11:07	10:39	05:24	18:54	15:39	05:39	09:24	10:54	03:24	23:24	23:54	09:24	00:39	11:54	02:39	02:24	08:24
	Last frame time	13:37	11:54	06:39	20:39	16:24	06:24	09:54	12:24	03:54	23:54	00:54	11:24	01:54	13:39	03:39	03:54	08:39
	Number of frames	6	5	5	6	3	3	3	5	3	3	3	5	5	6	4	4	2
	Expansion parameter	0, 0	4, 4	4, 4	0, 8	4, 4	8, 8	0, 0	0, 14	14, 14	4, 4	10, 10	14, 14	4, 4	16, 16	4, 4	4, 4	0, 0
De-projected solar distance (solar radii)		12–16	6–13	7–11	5–9	7–9	11–13	9–12	8–9	6–7	6–9	6–10	7–11	6–10	7–11	6–10	6–9	8–9
Maximum error of the triangulation (solar radii)		0.1	0.1	0.1	0.1	0.1	0.1	0.1	0.1	0.1	0.1	0.2	0.1	0.1	0.2	0.1	0.2	0.1
Adjacent CME		no	no	no	no	yes	no	yes	no	yes	no	yes	no	no	yes	yes	yes	no
Average velocity vector	Magnitude (km s^{-1})	376	958	576	388	598	401	1119	184	434	982	585	379	556	463	740	623	859
	Latitude (Stonyhurst)	7°	−31°	−7°	2°	−1°	4°	5°	3°	33°	30°	29°	−2°	16°	−2°	−13°	33°	2°
	Longitude (Stonyhurst)	3°	−2°	3°	1°	7°	−26°	−12°	−1°	6°	7°	31°	30°	14°	−4°	6°	8°	14°
$\overline{v_r}(\theta_j, \phi_k)$	Number of acceptable radial directions	20	105	46	136	137	26	73	3	58	350	82	35	132	127	16	138	128
	Minimum value of $\overline{v_r}(\theta_j, \phi_k)$ (km s^{-1})	344	945	549	350	585	355	1092	176	423	814	499	338	551	449	647	607	688
	Maximum value of $\overline{v_r}(\theta_j, \phi_k)$ (km s^{-1})	403	980	593	418	658	456	1161	194	447	1249	634	396	618	497	799	659	970
Latitudinal and Longitudinal ranges	$[\theta_1,\theta_p]$(Stonyhurst)	[−6°, 15°]	[−43°, −19°]	[−15, 4°]	[−10°, 16°]	[−20°, 14°]	[0°, 14°]	[−4°, 16°]	[−11°, 5°]	[28°, 38°]	[5°, 57°]	[18°, 38°]	[−13°, 8°]	[−5°, 45°]	[−19°, 16°]	[−29°, −11°]	[17°, 59°]	[−10°, 19°]
	$[\phi_1, \phi_p]$ (Stonyhurst)	[2°, 7°]	[−4°, 5°]	[−1°, 16°]	[−5°, 8°]	[1°, 11°]	[−33°, −23°]	[−15°, −7°]	[−10°, 17°]	[3°, 10°]	[−2°, 28°]	[27°, 41°]	[24°, 42°]	[10°, 27°]	[−21°, 4°]	[−2°, 11°]	[−18°, 16°]	[10°, 17°]

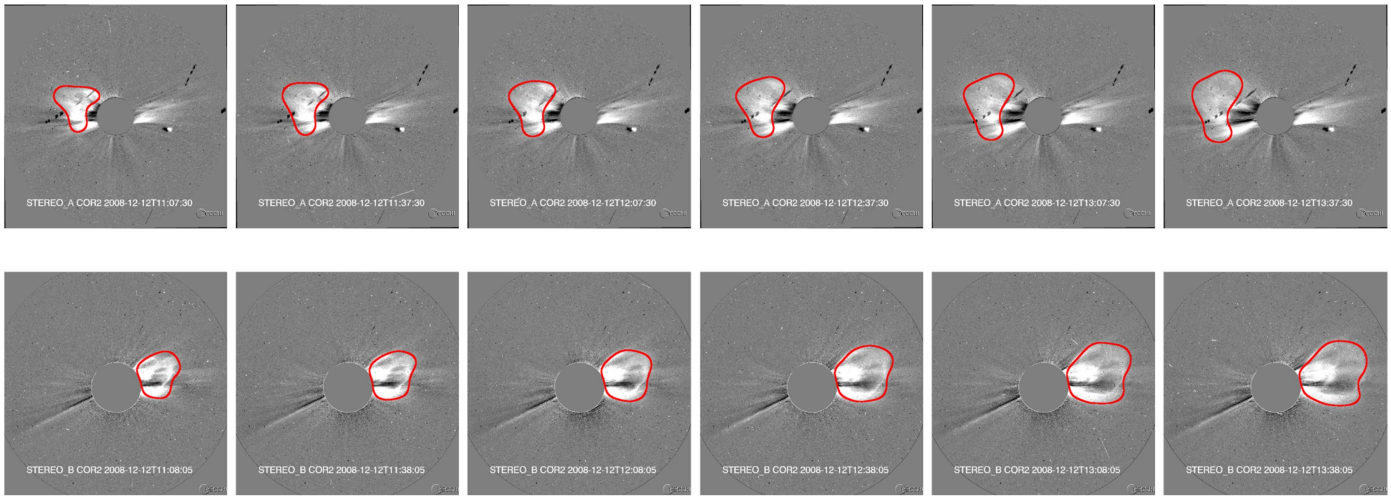

Figure 7. CME event observed on 2008 December 12 on COR2A (upper panels) and COR2B (bottom panels) FOVs. The red line indicates the CME segmentation obtained by CORSET.

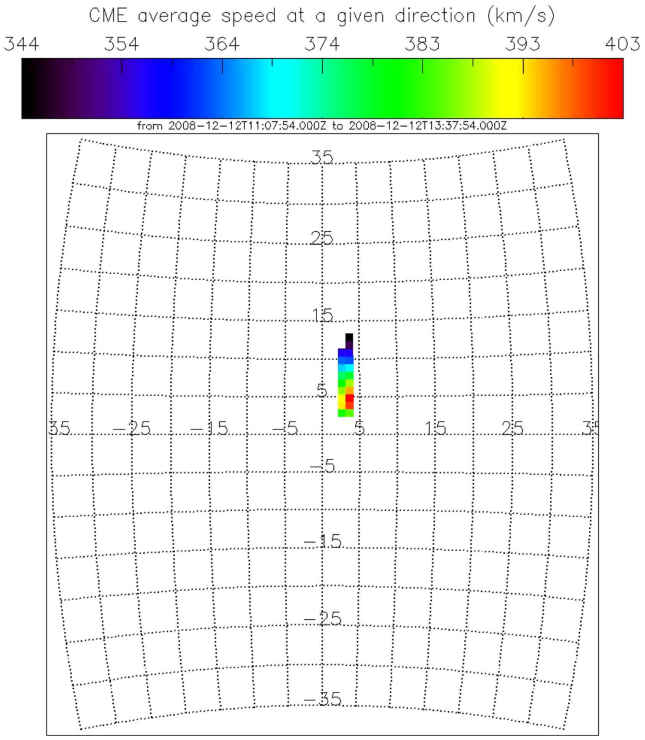

Figure 8. Radial speeds of the front of the CME event observed on 2008 December 12 as a function of latitude and longitude (in the Stonyhurst coordinate system), as derived by CORSET3D.

If we assume that this event continues propagating radially after 13:37 UT, it would be observed at Earth with its center in the negative side of the y axis of the Geocentric Solar Ecliptic (GSE) coordinate system. This assumption seems to be in agreement with the magnetic flux estimated by Howard & DeForest (2014). According to these authors, the corresponding magnetic structure reached Earth first in the negative portion of the y axis, i.e., westward of the Sun–Earth line.

A previous study from Liu et al. (2010) used triangulation in both *STEREO*/COR2 and *STEREO*/Heliospheric Imagers' FOVs to track this CME event along its evolution to Earth (see, e.g., Figure 9 in Liu et al. 2010). They identified two structures in the time-elongation maps constructed from running difference images along the ecliptic plane. They called these two structures "feature 1" and "feature 2," although they seem to be part of one complex CME structure, which is the one CME event considered in this work. Liu et al. (2010) found that the speed of both features ranged between 300 and 600 km s^{-1}, developing westward during their entire evolution from the Sun to the Earth.

Lugaz (2010) computed the direction of this complex event with respect to the Sun–Earth line using two different methodologies that require both *STEREO* Heliospheric Imagers. By using triangulation he obtained $3 \pm 4°$, and by using the tangent-to-a-sphere technique he derived a direction of propagation of $8 \pm 10°$ with respect to the Sun–Earth line.

Both Liu et al. (2010) and Lugaz (2010) computed the direction of propagation of the event at further distances from the Sun (from approximately 20 to 160 solar radii) than in our work. In spite of this, their results are in good agreement with ours within the error range: CORSET3D estimated the direction of propagation to be along an average longitude of 3°.

We found only one reference work indicating the main propagation latitude of this event (Liewer et al. 2015). According to that work, the propagation direction is 8° latitude (Stonyhurst). This is in good agreement with CORSET3D: 7° Stonyhurst.

3.2. Event #2: CME Event on 2010 April 3

The CORSET3D estimate of the magnitude of the average velocity vector of the CME observed by the twin *STEREO*/COR2 instruments on 2010 April 3 is 958 km s^{-1}. A comparison with results from previous works is summarized in Table 2. Colaninno (2012) computed the apex of the GCS model and fit the height–time profile with multiple polynomial functions. The de-projected speed they derived at ten solar radii is similar to the result found in this paper. Rollett et al. (2012) studied this event using only the two Heliospheric Imagers onboard *STEREO A*. For the determination of the de-projected speed, they used two methods based on observations from only one viewpoint: the fixed Φ technique (Rouillard et al. 2008) and the harmonic mean method (Lugaz et al. 2009). Although both methods were derived at distances much further from the Sun than in the

Table 2
Speeds and Direction of Propagation Derived with Different Methodologies for the CME Event Observed on 2010 April 3

Method and reference	COR2 A		COR2 B		De-projected speed (km s^{-1})	Latitude (HEE)	Longitude (HEE)	Coverage
	Speed (km s^{-1})	PA (deg)	Speed (km s^{-1})	PA (deg)				
CORSET3D	956	97	975	263	958	−24°	0°	average up to 13 solar radii
GCS (Colaninno 2012)	809	⋯	800	⋯	917	−19°	6°	De-projected speed at 10 solar radii
Triangulation (Liu et al. 2011)	⋯	⋯	⋯	⋯	[800–1000]	⋯	[−10°, 15°]	COR2, HI1 and HI2 FOVs
GCS (Liewer et al. 2015)	⋯	⋯	⋯	⋯	829	−19°	3°	COR FOV
GCS (Möstl et al. 2014)	⋯	⋯	⋯	⋯	829	⋯	4°	average up to 16.5 solar radii
Fixed- Φ (Rollett et al. 2012)	⋯	⋯	⋯	⋯	829 ± 122	⋯	3° ± 4°	HI1 and HI2 FOVs
Harmonic Mean (Rollett et al. 2012)	⋯	⋯	⋯	⋯	854 ± 100	⋯	−25° ± 10	HI1 and HI2 FOVs
CACTus (*)	833	115	833	251	⋯	⋯	⋯	COR2 FOV
SEEDS (*)	810	130	929	237	⋯	⋯	⋯	COR2 FOV

Table 3
Speeds and Directions of Propagation Derived with Different Methodologies for the CME Event Observed on 2010 April 8

Method and reference	COR2 A		COR2 B		De-projected speed (km s^{-1})	Longitude (HEE)	Latitude (HEE)	Coverage
	Speed (km s^{-1})	PA (deg)	Speed (km s^{-1})	PA (deg)				
CORSET3D	512	103	576	277	576	3°	−1°	Average up to 11 solar radii
GCS (Colaninno 2012)	421	⋯	425	⋯	469	−2°	−3°	De-projected speed at 10 solar radii
GCS (Liewer et al. 2015)	⋯	⋯	⋯	⋯	511	−9	−8	COR2 FOV
CACTus (*)	520	92	543	267	⋯	⋯	⋯	COR2 FOV
SEEDS (*)	478	100	492	251	⋯	⋯	⋯	COR2 FOV

CORSET3D analysis, the speed found is within the range of the corresponding results from this paper if we take into account the errors provided by the authors.

CORSET3D found this CME to be directed significantly below the ecliptic plane (−24° in HEE). Colaninno et al. (2013) applied the GCS method at about 10 solar radii and found −19° of latitude (HEE). Liewer et al. (2011) stated that the source region of this CME is an active region located at −25° of latitude and that this latitude is kept in the trajectory. Although the latitudinal position of this event does not comply with the assumption #1 described in Section 2.4, the errors on the speed and longitudinal position are expected to change only slightly due to the geometry of the problem (see more details in Liewer et al. 2011). The angle between the CME propagation direction and the ecliptic introduces an error on the latitude so that its value as derived from triangulation is further away from the ecliptic than it would be without this effect.

The longitude of the CME propagation found using CORSET3D is −2° of the Sun–Earth line in a range of up to 12 solar radii. Many previous papers also computed this parameter. For instance, Colaninno et al. (2013) found 6° at 10 solar radii using the GCS method, and Möstl et al. (2011) found a longitude of 4° up to 16 solar radii. Two other articles extended the analysis at much further distances from the Sun including the observation from the Heliospheric Imagers. Liu et al. (2011) reported the direction of propagation as a function of time. Considering only the time period covered by CORSET3D, the CME longitude starts at about −10° and gradually develops toward positive values, reaching about 10° at the end. At further distances from the Sun, the results from Liu et al. (2011) range mainly from 0° to 15° of longitude. Rollett et al. (2012), using exclusively the data from the Heliospheric Imagers, obtained similar results using the fixed Φ method. The same authors also applied the harmonic mean method and their results are in disagreement with all the others mentioned here. In summary, the longitude found for this CME using CORSET3D seems to agree with most previous works.

3.3. Event #3: CME Event on 2010 April 8

The linear speeds reported by both CORSET3D and other methodologies for the CME observed on 2010 April 8 by the *STEREO*/COR2 coronagraphs are shown in Table 3. Due to the limitations of CORSET3D, the time window we used is smaller than in the studies mentioned here (while CORSET3D was only able to track the event for less than two hours, the automatic catalogs tracked it for more than three).

As was the case with Event #1, the first two hours of the CME development in the COR2 FOVs were ignored because the NARD decreased dramatically when those frames were included in the analysis. This is probably due to the small projected area of the CME observed in the coronagraph during the early stages of its development.

As seen in Table 3, the speeds derived on each coronagraph FOV by CORSET tend to be higher, CACTus (COR2 A) being the exception. The height–time scatter plot obtained from CORSET determinations (not shown here) exhibits a high correlation, without outliers. On the other hand, the corresponding scatter plot constructed upon SEED determinations (not shown here) shows that the first height–time points for both coronagraphs do not linearly fit with the remaining ones (indicative of an acceleration phase during the early stages of the development). As a result, the speeds

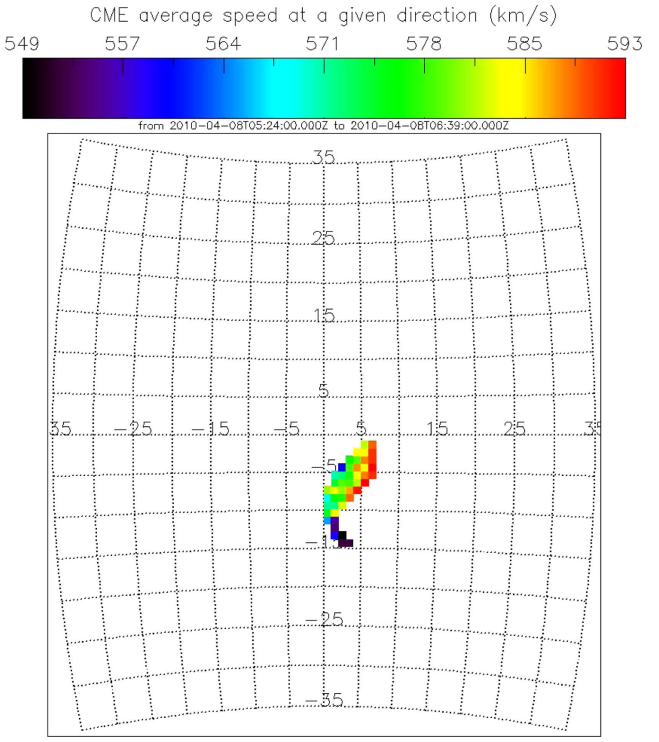

Figure 9. Radial speed of the CME front as a function of latitude and longitude (in the Stonyhurst coordinate system). The CME shown here was observed on 2010 April 8.

derived from the linear fit are smaller than they should be. We do not have height–time information available for the remaining references.

The difference between the longitudinal directions of propagation found by Colaninno (2012) using the GCS model and CORSET3D is 5°. This value lies inside the general error range found by Mierla et al. (2010), who compared results from different methodologies for several CMEs. Regarding the de-projected speed, the results from CORSET3D appear higher than from the other methods. This difference in speed agrees with the expected errors from the DALE effect discussed in Section 2.3.

Figure 9 shows the distribution of the radial speed of the CME front as a function of latitude and longitude as derived by CORSET3D. We notice in this figure that the portion of the event developing farthest from the Sun–Earth line exhibits a higher radial speed (reddish dots). The northernmost FP on the last frame analyzed is at 11.9 solar radii while the southernmost FP is only at 10.8 solar radii (not shown here). If we take into account that the triangulation error is less than 0.1 solar radii for this case, this difference cannot be ignored, and hence suggests that the CME front is indeed moving faster at the northernmost ARD (the difference is speed is approximately 50 km s^{-1}).

Moreover, as the CME is observed close to the solar equator, the corresponding ICME/MC should have been observed at Earth close to the ecliptic plane (under the assumption that the front of the CME keeps the same distribution of the radial profile all along its development up to the Earth). The corresponding ICME was studied in previous works but, unfortunately, its position in relation to the ecliptic plane could not be determined (Colaninno 2012; Braga 2015). The reason was simply because this event could not be fitted by a flux rope

Table 4
Speeds and Directions of Propagation Derived with Different Methodologies for the CME Event Observed on 2010 May 23

Method and reference	COR2 A		COR2 B		Speed (km s^{-1})	Latitude (HEE)	Longitude (HEE)	Coverage
	Speed (km s^{-1})	PA (deg)	Speed (km s^{-1})	PA (deg)				
CORSET3D	393	78	467	294	388	4°	1°	up to 9 solar radii
GCS Lugaz et al. (2012)	362	⋯	378	⋯	[300–400]	0°	10°	9.5 solar radii
CACTus (*)	378	79	390	277	⋯	⋯	⋯	?
SEEDS (*)	363	84	365	277	⋯	⋯	⋯	up to 12 solar radii

Table 5
Speeds and Directions of Propagation Derived with Different Methodologies for the CME Event Observed on 2010 May 24

Method and reference	COR2 A Speed (km s^{-1})		COR2 B Speed (km s^{-1})		De-projected speed (km s^{-1})	Latitude (HEE)	Longitude (HEE)	Coverage
	Speed (km s^{-1})	PA (deg)	Speed (km s^{-1})	PA (deg)				
CORSET3D	766	69	646	280	598	0°	7°	up to 9 solar radii
GCS Lugaz et al. (2012)	650	⋯	650	⋯	[500–700]	−2°	26°	at 9.5 solar radii
CACTus (*)	480	94	⋯	⋯	⋯	⋯	⋯	?
SEEDS (*)	504	102	536	273	⋯	⋯	⋯	up to 12 solar radii

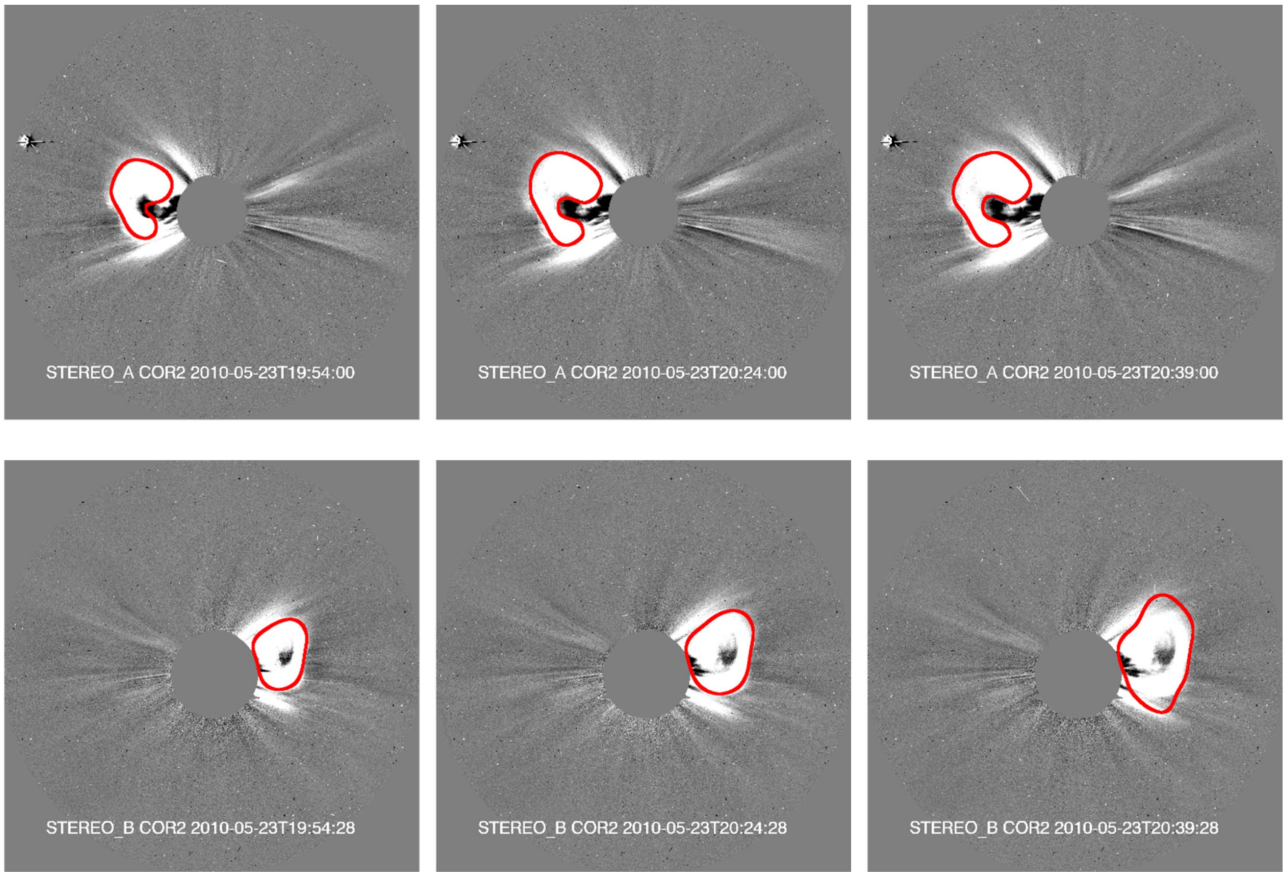

Figure 10. CME observed on 2010 May 23 on COR2A (upper panels) and COR2B (bottom panels) FOVs.

Table 6
Speeds and Directions of Propagation Derived with Different Methodologies for the Two CME Events Observed on 2010 August 1

Method	CME #6			CME #7			Coverage
	De-projected speed (km s^{-1})	Longitude	Latitude	De-projected speed (km s^{-1})	Longitude	Latitude	
CORSET3D	401	−26°	4°	1119	−12°	5°	COR2
GCS (Temmer et al. 2012)	650 ± 150	−20 ± 10°	9 ± 5°	1160 ± 200	−28 ± 5°	20 ± 5°	COR1 and COR2
Triangulation (Liu et al. 2012)	732	−23°	⋯	1138	−19°	⋯	COR2 and HI1

Note. The latitude and longitude values are given in Stonyhurst coordinates.

near to Earth (although close to the Sun, the CME could be fitted by a flux rope model using the GCS model).

3.4. Events #4 and #5: CME Events on 2010 May 23 and 2010 May 24

These two events have been studied by Lugaz et al. (2012) using the GCS model technique. A summary of their results, along with those from both the CACTus and the SEED CME catalogs, and CORSET3D, are displayed in Tables 4 and 5. Results derived using CORSET3D for the first event are in good agreement with those from Lugaz et al. (2012) for both speed and direction (see Table 4). The CORSET segmentation of this CME on both COR2-A and COR2-B is shown in Figure 10.

For the second event (CME on 2010 May 24), the difference in the determination of the direction of propagation derived by Lugaz et al. (2012) and by CORSET3D is small for the latitude (only 2°) but quite large for the longitude (19°). However, the de-projected speed derived from CORSET3D falls within the speed range computed by Lugaz et al. (2012) (see Table 5). One plausible reason for the discrepancy in the longitude is that the GCS method has many free parameters and hence there is no unique way to fit the model to the CME observations.

3.5. Events #6 and #7: two CME Events on 2010 August 1

The two CMEs observed on 2010 August 1 by the *STEREO* twin S/C were ejected approximately toward Earth, eastward of the Sun–Earth line and northward of the ecliptic plane. The parameters determined by CORSET3D for these two events are displayed in Table 6 along with those from others works obtained using different methodologies.

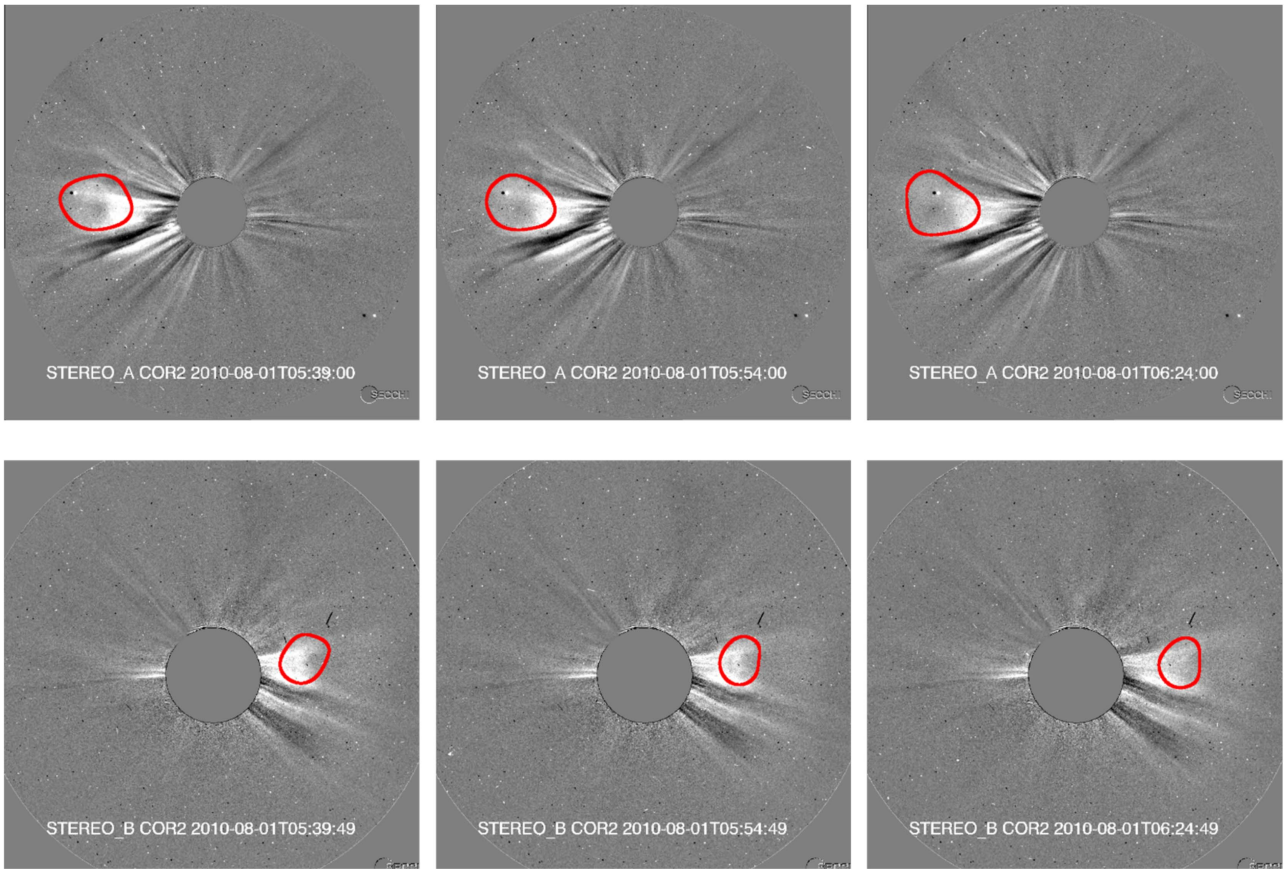

Figure 11. First CME observed on 2010 August 1 on COR2A (upper panels) and COR2B (bottom panels) FOVs.

The de-projected speed derived by CORSET3D for event #6 is significantly smaller than that calculated with other methodologies. One plausible explanation for the difference observed is the extremely diffuse nature of the CME front (see Figure 11). The direction of propagation of this CME, however, is in quite good agreement with all the methods. On the other hand, the speed calculated for the CME #7 (Figure 12) exhibits a very good agreement, although there is a considerable difference in the direction of propagation (CORSET3D results point to values of both latitude and longitude closer to zero).

According to Temmer et al. (2012), the first CME originated in a small active region (NOAA AR 11094), which was located at $-14°$ longitude, $14°$ latitude. For the second CME, the origin is another active region (NOAA AR 11092) located at $-35°$ longitude, $20°$ latitude. Note that the position of the active region of the second event is northward and eastward of the first. The longitude of the direction of propagation of the two events derived by Temmer et al. (2012) better matches the solar source location than the corresponding results derived from CORSET3D. In particular, for CME #7, the difference between the CORSET3D and the GCS method exceeds the general error ($10°$) found by Mierla et al. (2010). Another point that can be noticed for CME #7 is that CORSET3D's longitude is closer to zero than the others. A possible explanation for the disagreement could be the DALE effect. As discussed in Section 2.4, longitudes derived with a triangulation method tend to be smaller than actual longitudes, the error increasing with larger actual longitudes (note that Liu et al. 2012 using a triangulation method also derived a much smaller value; see, e.g., Table 6).

3.6. Event #8: CME Event on 2011 March 25

CORSET3D results are displayed in Table 7 along with those from the CACTUS and SEED CME catalogs, and Colaninno (2012), who also studied this event. As in all previous events analyzed here, the de-projected speed is the magnitude of the average velocity vector (Section 2.3). The plane-of-sky speed indicated for each coronagraph corresponds to the speed of the fastest moving element (at position angle PA). The longitude and latitude are taken from the average velocity vector calculated as explained in Section 2.3.

Colaninno (2012) computed an average de-projected speed of about 47 km s^{-1} during the first 8 hr of its development (i.e., between 01:25 UT and 09:25 UT) using the multiple polynomial function approach from Wood et al. (2009). As specified in Table 1, the segmentation from CORSET starts later: at 10:54 UT (see Figure 13). The result from Colaninno (2012) is in disagreement with the speed map derived from the CORSET3D analysis, which shows speeds higher than 150 km s^{-1}. This is most likely due to the different time window used for the analysis of the event. The CME was observed to be accelerating while propagating on the COR2 FOVs. Therefore, the speed of CORSET3D is expected to be higher because it was observed at a later time period.

Note also that the difference found for the derived longitudes by the GCS model and CORSET3D is very significant and outside the error range found by Mierla et al. (2010). We conjecture that the most likely reason for this difference is that the region chosen to fit the GCS model comprises a different portion of the CME as segmented by CORSET. A careful inspection of the results from Colaninno (2012) shows that

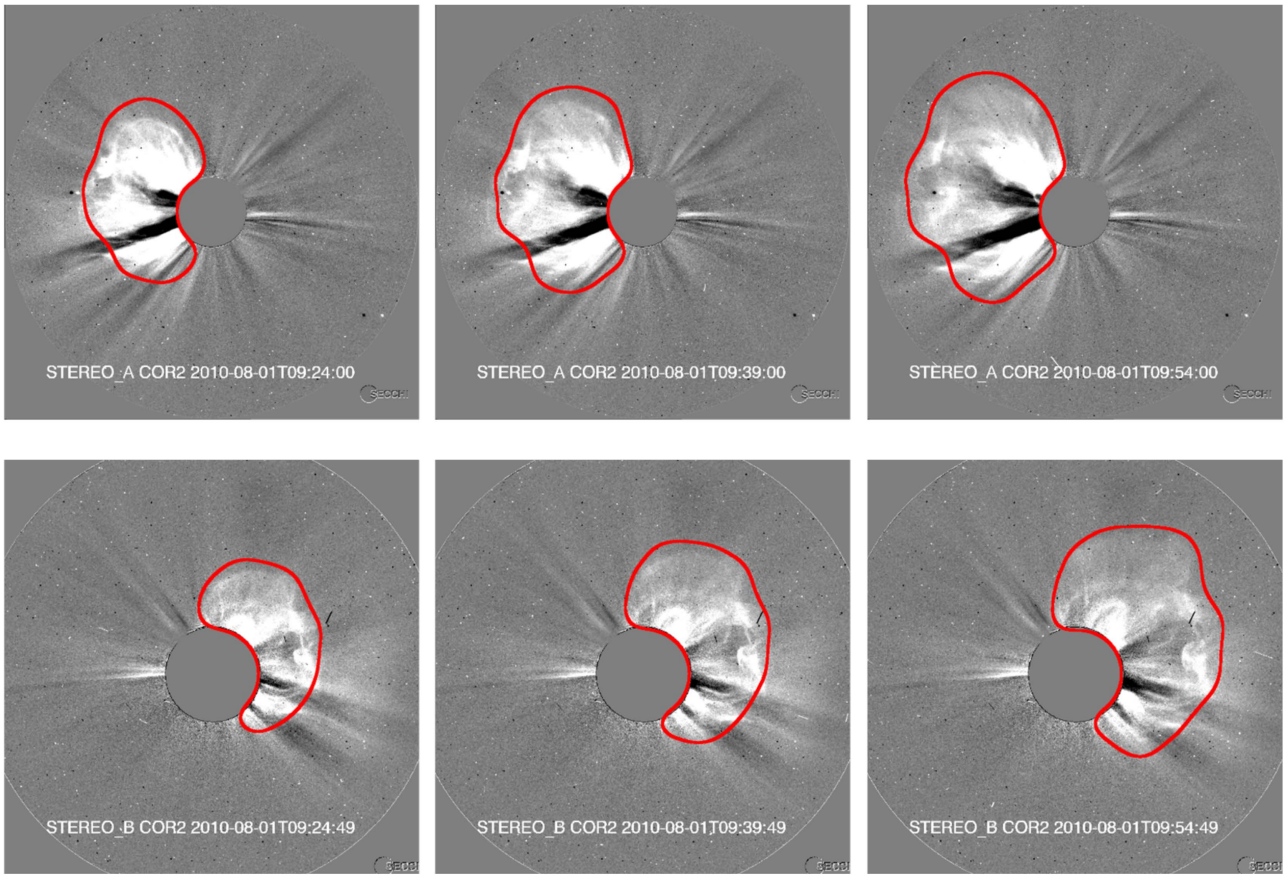

Figure 12. Second CME observed on 2010 August 1 on COR2A (upper panels) and COR2B (bottom panels) FOVs.

only the core of the CME is included on the application of the model. On the other hand, and as can be seen in Figure 13, the leading edge of the event was included in the CORSET segmentation.

Moreover, the GCS model fitting might have been influenced by the superposition with another CME in the LASCO-C3 FOV. To fit the GCS model, Colaninno (2012) used a set of three frames: one showing the CME at a height of 10 solar radii (11:54 UT), the second at 20 solar radii (15:24 UT), and the last one at 50 solar radii (11:29 UT on the following day using the HI-1 FOV). As seen on the LASCO-C3 FOV, the CME under study here shows up superposed in the line of sight by another halo CME, which was ejected during the first hours of 2011 March 26 (this event is directed away from Earth). On the COR2A and COR2B FOVs, there is no significant superposition of both CMEs since the projections are located in opposite position angles, approximately 180° from each other. Since CORSET3D does rely only on COR2 observations, the analysis in unlikely to be biased by the CME directed away from the Earth. Since the fitting of the GCS model is done by visual inspection and relies on LASCO-C3 observations, the superposition might have biased adjustments of the GCS parameters.

3.7. Events #9 Through #12: CME Events between 2011 September 6 and 2011 September 9

In the period between 2011 September 6 and 2011 September 9, four Earth-facing CME events were recorded. We group them together because their time lag is short. The CORSET3D derived parameters are listed in Table 1. CME #10 is the one that extends closer to the coordinates (0°, 0°); see, e.g., Figure 14. The remaining CMEs are distant from this point in at least one of their coordinates.

As can be seen in Table 1, we notice that the CME #10 is considerably faster than CME #9, which was ejected about 20 hr earlier. Depending on the acceleration and/or deceleration of these CMEs beyond the outer limit of COR2 FOV, they may have interacted with each other. If both CMEs developed at constant speed during their evolution, the collision would have occurred approximately 20 hr after the CME #10 ejection, i.e., at about 0.4 au from the Sun.

Möstl et al. (2014) found a direction of propagation of about 34° (Stonyhurst) westward of the Sun–Earth line. This result diverges from the longitude derived by CORSET3D from the average velocity vector by more than 20°. As can be noted in Figure 14 (upper right panel), this difference is reduced to less than 10° when considering the ARD at the northernmost portion of the CME. This CME has an inclined profile in the ARD distribution ranging more than 20° in longitude. We interpret that this inclination is associated with the rotation angle parameter defined in the GCS model. In the specific case of this CME, Möstl et al. (2014) did not report this parameter.

3.8. Event #16: CME Launched on 2011 October 22

The presence of two other CME events on 2011 October 22 in close angular range in the FOV of the COR2 coronagraphs complicated the analysis of the event of interest. The event under analysis here was first seen at 01:24 UT and 01:54 UT at position angles ∼30° and ∼330° in the FOV of the COR2A and COR2B instruments, respectively. The other two events

Table 7
Speeds and Directions of Propagation Derived with Different Methodologies for the CME Event Observed on 2011 March 25

Method and coverage	COR2 A		COR2 B		De-projected speed (km s^{-1})	Latitude (HEE)	Longitude (HEE)	Coverage
	Speed (km s^{-1})	PA (deg)	Speed (km s^{-1})	PA (deg)				
CORSET3D	158	68	202	287	184	10	−1	COR2 FOV up to 9 solar radii
GCS Colaninno (2012)	100	⋯	142	⋯	47	3	−27	COR2 and HI-1 FOV
CACTus	⋯	⋯	235	262	⋯	⋯	⋯	COR2 FOV
SEEDS	199	104	171	261	⋯	⋯	⋯	COR2 FOV

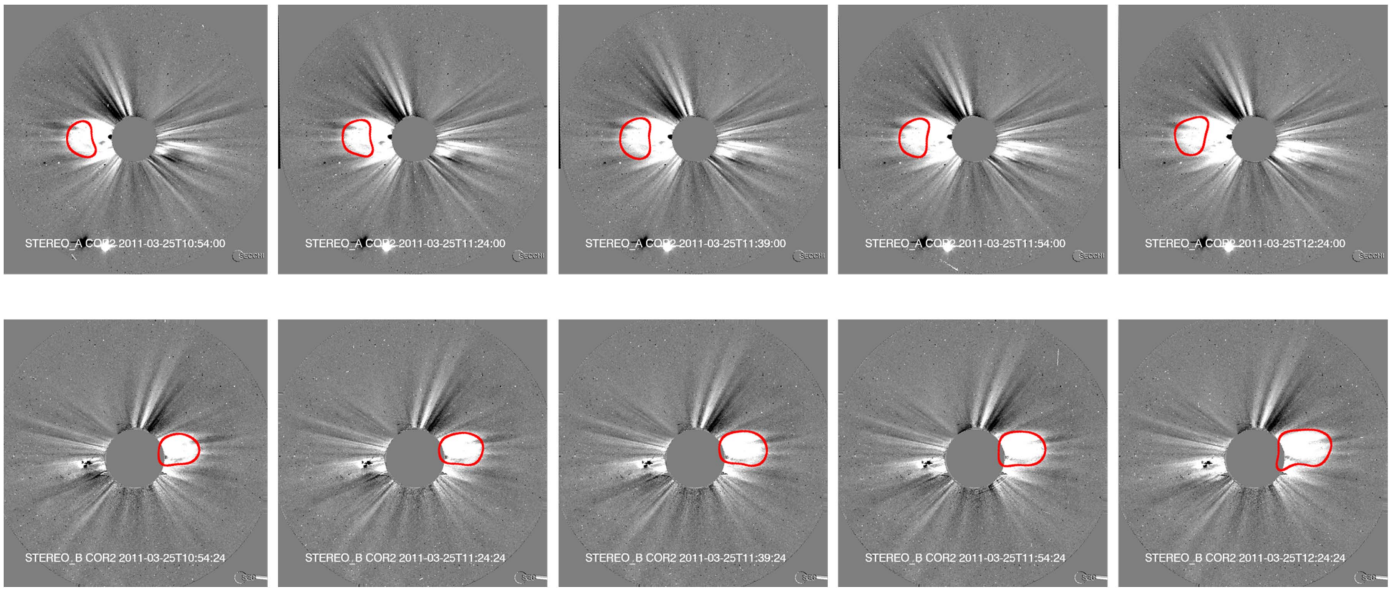

Figure 13. CME observed on 2011 March 25 on COR2A (upper panels) and COR2B (bottom panels) FOVs.

were ejected some hours before. One of these events (i.e., the one first seen at 19:24 UT on 2011 October 21) appears partly superposed in the line of sight with the event of interest, and exhibits an angular width of at least 60°, developing at position angles ∼130° and ∼220° in COR2A and COR2 B, respectively. The other event (i.e., the one first seen at 22:24 UT on 2011 October 21) is narrower (∼30°) and shows up fully superposed in the line of sight with the event of interest, developing at position angles ∼10° and ∼350° in the COR2A and COR2B FOVs, respectively.

We show in Figure 15 the segmentation of the event of interest as obtained by CORSET3D in a restricted time sequence of COR2A (top panel) and COR2B (bottom panel) images. The two events that complicated the analysis show up in the frames as dark regions (signature of their presence in the base image used, taken at 01:24 UT).

As can be noticed in Figure 15, the event on the north is particularly disturbing for the segmentation. To our understanding, the selection of the CME front of interest seems to be self-consistent between *STEREO A* and *STEREO B*, i.e., the same feature appears to be segmented by CORSET in the FOV of both instruments. Likewise, the segmentation seems to be consistent in time, the exception being the last COR2B frame.

The magnitude of the average velocity vector derived by CORSET3D for this event is 623 km s^{-1} (Table 1). The derived direction of propagation of the bulk of the event is 33° latitude, 8° longitude (Stonyhurst). Möstl et al. (2014) found the event propagating in a direction of 19° longitude (Stonyhurst) using the GCS model, with an average speed of 692 km s^{-1}.

We note that the direction of propagation derived by Möstl et al. (2014) matches the portion of the radial speed distribution that is closest to the ecliptic plane, as can be seen in Figure 16. In this region, the derived longitude from CORSET3D is 15° and the radial speed is 637 km s^{-1}. No information about the latitude of the CME was found in previous studies.

4. Discussion

CORSET3D allows us to derive the radial speed of a CME at every direction comprised by its front. For a given CME, we have constructed the distribution of the average velocity as a function of latitude and longitude. From the set of radial velocity vectors extracted for each CME, we derived the average velocity vector characterizing the linear velocity of the event. For the CME sample studied here, the linear velocities measured ranged from 184 to 1119 km s^{-1}. The average difference between the minimum and maximum radial speeds for each CME was about 90 km s^{-1}. Although this difference lies within the error range of 100 km s^{-1} from Mierla et al. (2010), this number illustrates the possibility of using CORSET3D to estimate the differences in the de-projected radial speed at different angular positions in a future work. This information might be used as a way to study the CME deformations (see, e.g., Savani et al. 2010).

The latitude and longitude of the average velocity vectors ranged from −31° to 33° and from −26° to 31°, respectively. The average latitude of the CME sample was 6° and the longitude is 5° as derived from the average velocity vector in Stonyhurst. This result suggests that the CME events associated with MCs observed at Earth exhibit a direction of propagation close to the Sun–Earth direction if we take into account the error of 10°.

CORSET3D was not able to track any CME event of the sample studied here in the whole FOV of the COR2 instruments. In some cases, the range covered was even lower than 10 solar radii (the COR2 FOV extends up to 15 solar radii in nominal conditions). In the majority of the cases, the resulting CME segmentation from CORSET at the very early stages of the event development were discarded for 3D reconstruction purposes. The corresponding reconstructed front exhibited a relatively high error, most likely due to the small number of ARDs when the event appearance was small.

In all cases, we forced CORSET to run up to the outer limit of the coronagraphs' FOVs. Unfortunately, the area segmented in the last frames (typically the last two or three frames) was not consistent with the CME definition because extensive regions of the background scene were included. These frames were all ignored in the analysis. The improper segmentation occurs because the texture of the CME becomes pretty similar to that of the background at large distances, and hence the

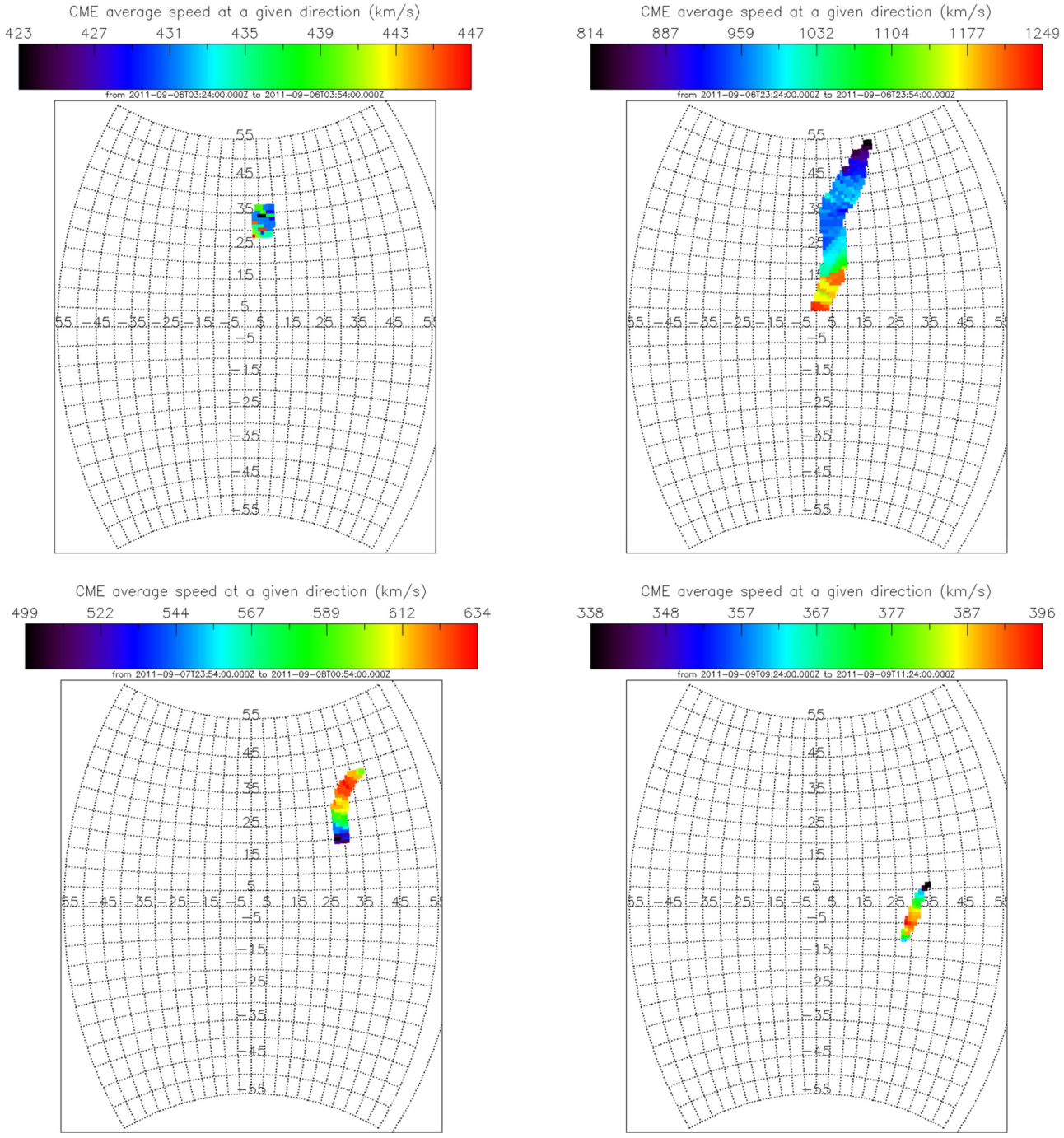

Figure 14. Linear radial speed distribution of four CME events observed between 2011 September 6 and 2011 September 9. Upper left panel: CME #9. Upper right panel: CME #10. Bottom left panel: CME #11. Bottom right panel: CME #12.

statistical test the algorithm performs to distinguish between foreground and background fails. The number of "useful" frames is shown in Table 1 and ranges from 2 to 6, the average being 4.64, the median being 4 and the standard deviation 1.3. This limitation of CORSET3D is more significant for fast CMEs due to the low number of frames available. In spite of this, the magnitude of the fastest CME studied here was found to be consistent with results from previous works using different methodologies.

The CORSET algorithm requires upon initialization the setting of the so-called expansion parameter Q to control the degree of expansion of the CME area found in the preceding image before proceeding to segmentation (as introduced in Section 2.1). The values adopted for each event analyzed on each COR2 instrument are shown in Table 1 (sixth row). This parameter ranges from 0 to 60 (0 means no expansion; otherwise the higher the parameter, the lower the expansion). We adopted $Q = 4$ for 14 (41%) of the 34 cases (17 CMEs for each spacecraft). This particular selection of the parameter matches that of 67% of an extensive set of CMEs analyzed in a previous work on LASCO-C3 FOV (Braga et al. 2013). In 8 cases (i.e., 24%), $Q = 0$ was adopted. Note that using $Q = 0$ or $Q = 4$ produced consistent CME tracking results in ∼65% of the cases. The remaining parameter values used were: 14

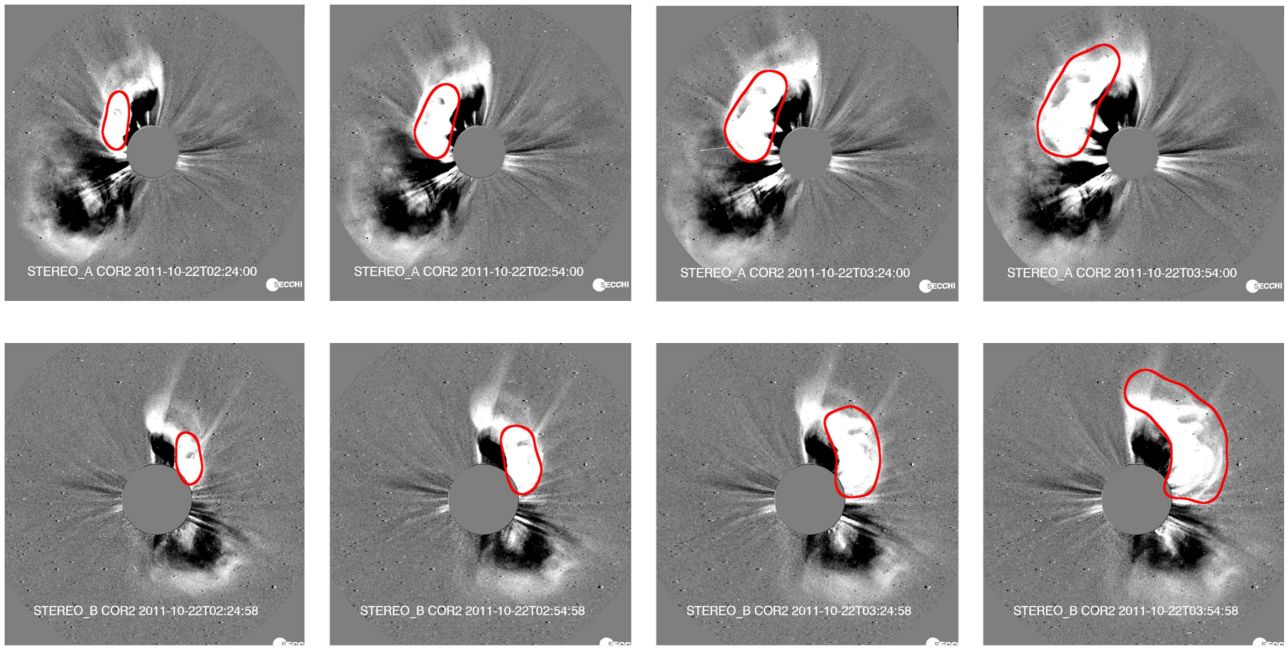

Figure 15. CORSET3D segmentation of the CME event observed on 2011 October 22 by COR2A (upper panels) and COR2B (bottom panels).

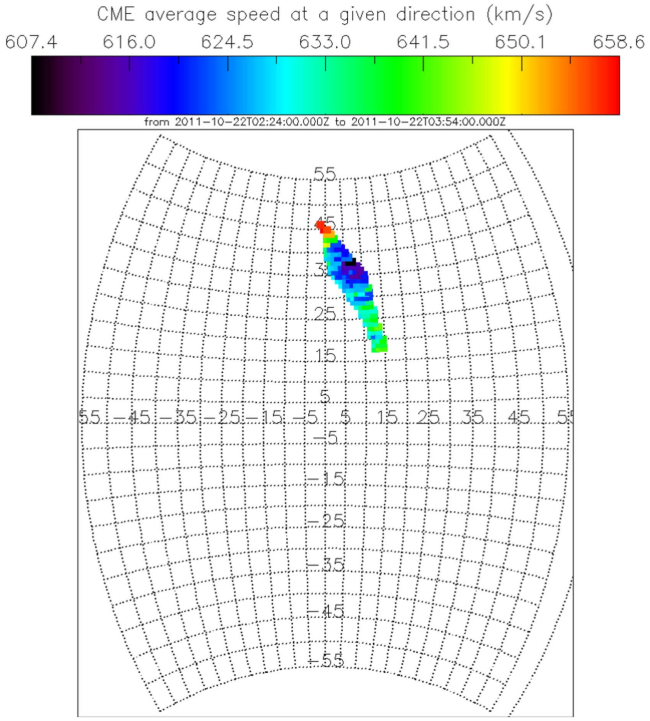

Figure 16. Radial speed of the CME front for event #16 (2011 October 22) as a function of latitude and longitude (in the Stonyhurst coordinate system).

(5 cases, 15%), 8 (3 cases), 10 and 16 (each one used twice, 6% of the cases). For some cases, we had to set Q at a different value for a given CME for each spacecraft. In particular, when $Q = 0$, the texture of the CME feature is reevaluated in a region that matches the CME segmentation in the previous frame (i.e., no expansion). It is interesting to notice that in Braga et al. (2013) none of the 57 CMEs studied was tracked using parameter $Q = 0$. This value was adopted here after trying many other values of Q from the same reference (such as 8, 10, 14 and 16) without proper results. For the events studied in this work, the higher expansion ratio adopted (i.e., $Q = 4$) seems to be set mostly for events that are relatively brighter than the remaining cases studied here. Examples of this case include CMEs #2, #3 and #13. On the other hand, lower values of expansion ratio (i.e., higher Q) are set in those cases in which the CME is seen with relatively low brightness (see, for example, CMEs #1 and #7). Since the list of CME events analyzed here is small, a detailed study is necessary to confirm the apparent trend found.

For the CME events sample studied in this work, we found previous studies for only 10 events. An overview of the comparison of results is shown in Table 8. The cases whose results disagree with all the previous studies (as detailed in Sections 3.1 throughout 3.8) are indicated in the last column (from left to right). The criteria used to declare disagreement are (1) a difference of more than 100 km s^{-1} for the speed and (2) a difference in angle higher than 10° (following the general result from an extensive comparison of propagation directions derived from several methods by Mierla et al. 2010). In the case of the radial speeds, we considered the value of $\overline{v_r}(\theta_j, \phi_k)$ that produces the minimum difference. If the speed from CORSET3D was higher (lower) than the speed from a previous reference, we took the minimum (maximum) value of $\overline{v_r}(\theta_j, \phi_k)$. For the latitudinal and longitudinal ranges, we took the value closest to the results from previous references.

If we take into account the directions derived from the average velocity vector, the CORSET3D longitude determination of four CMEs (CMEs #5, #8, #10, and #16) and the latitude of one other (CME #7) do not agree. We also compared the latitudinal and longitudinal angular spans (as described in Section 2.3) with previous works. In this case, we found one event with a discrepancy in latitude (CME #7) and another two (CME #5 and #8) in longitude. One possible reason for the differences is the presence of an adjacent CME, i.e., another CME not necessarily earthward directed was observed at least on COR2A or COR2B in close timing and/or position to the earthward-directed CME. In particular, the CME events observed on 2010 May 24 and August 1 (second event) are examples of this case.

Table 8
Summary of Comparison of Events Analyzed by CORSET3D and Other Methods Such as the GCS and Triangulation

#	Event	Parameter	CORSET3D	GCS	Triangulation	Discrepancies
1	2008 Dec 12	De-projected speed	376 km s^{-1}	497 km s^{-1}	[300–600]	⋯
		Long	2°	8°	3°	⋯
		Lat	8°	8°	⋯	⋯
2	2010 Apr 3	De-projected speed	958 km s^{-1}	917 km s^{-1} (Co) 829 km s^{-1} (Li)	[800–1000] km s^{-1}	⋯
		Long	0°	−6° (Co) 3° (Li)	3°	⋯
		Lat	−24°	−19° (Co) −19° (Li)	−10° 15°	⋯
3	2010 Apr 8	De-projected speed	576 km s^{-1}	469 km s^{-1} (Co) 511 km s^{-1} (Li)	⋯	⋯
		Long	3°	−2° (Co) 9° (Li)	⋯	⋯
		Lat	−1°	−3° (Co) 8° (Li)	⋯	⋯
4	2010 May 23	De-projected speed	388 km s^{-1}	[300–400] km s^{-1}	⋯	⋯
		Long	1°	10°	⋯	⋯
		Lat	4°	0°	⋯	⋯
5	2010 May 24	De-projected speed	598 km s^{-1}	[500–700] km s^{-1}	⋯	⋯
		Long	7°	26°	⋯	*, #
		Lat	0°	−2°	⋯	⋯
6	2010 Aug 1	De-projected speed	401 km s^{-1}	650 km s^{-1}	732 km s^{-1}	*, #
		Long	−26°	−19°	−23°	⋯
		Lat	1°	5°	⋯	⋯
7	2010 Aug 1	De-projected speed	1119 km s^{-1}	1160 km s^{-1}	1138 km s^{-1}	⋯
		Long	−12°	−26°	−19°	⋯
		Lat	0°	17°	⋯	*, #
8	2011 Mar 25	De-projected speed	184 km s^{-1}	47 km s^{-1}	⋯	*, #
		Long	−1°	−27°	⋯	*, #
		Lat	10°	3°	⋯	⋯
10	2011 Sep 6	De-projected speed	982 km s^{-1}	1160 km s^{-1}	⋯	*
		Long	7°	34°	⋯	*
		Lat [?]	23°	⋯	⋯	⋯
16	2011 Oct 22	De-projected speed	623 km s^{-1}	692 km s^{-1}	⋯	⋯
		Long HEE)	5°	19°	⋯	*
		Lat	28°	⋯	⋯	?

Note. Details about each event are discussed in sections 3.1 through 3.8. All results indicated in this table are given in the HEE coordinate system. Discrepancies with previous results are indicated with the symbols "*," "#," and "?" in the last column of the corresponding row: "*" refers to the comparison with the velocity vector, "#" indicates disagreement in $\overline{v_r}(\theta_j, \phi_k)$, and "?" points out those cases that were not covered in any previous study discussed in this paper. For some events, GCS results from both Colaninno (2012) and Liewer et al. (2015) are available. "Co" and "Li" between parentheses indicates the first and second reference, respectively.

This limitation arises from the use of the base-difference images. The brightness of the adjacent CMEs forms dark regions on the sequence of CME images. As a result, the texture of those regions becomes completely different from the remaining areas of the CME, resulting in their exclusion from the region segmented by CORSET. Future studies should attempt to overcome this limitation using techniques such as dynamic signal separation (see, e. g., Morgan et al. 2012).

The remaining case with discrepancy is the CME launched on 2011 March 25. We found only one previous reference on this event (Colaninno 2012) and our inspection of the coronagraph images from COR2 and LASCO suggests that there are two different CMEs (the earthward-directed CME plus another later event) and that the application of the GCS method is possibly biased by the superposition of the two events.

With regard to the comparison of the magnitude of the average velocity vector derived by CORSET3D with previous works, we found that among the 10 events previously studied, three of them exhibited significant differences (CMEs #6, #8, and #10). If the comparison is done for the speed range, the number of discrepancies is two (CMEs #6, and #8). We considered the difference in speed significant when it is higher than 100 km s^{-1}. This limit value is approximately 15% of the average CME speed found here.

The limitations of CORSET3D are twofold, which are inherited from both CORSET and Sunloop. As for limitations inherited from the former, the CME segmentation is for instance not reliable when multiple CMEs are observed in close timing and location. In particular, if the background includes parts of another CME, a kind of ghost effect exists in the primary CME, and hence the resulting CME front may be contaminated and contain spurious features. As for limitations inherited from the 3D reconstruction approach utilized, it is worth noting that the CME main direction of propagation needs to be close to the Sun–Earth line (or approximately equidistant from the two observers) in order to reduce the error of the method. Although CME events ejected toward either *STEREO A* or *B* were not analyzed here, CORSET3D is able to analyze these cases. The drawback of CORSET3D (and of any other methodology based on triangulation and tie-pointing) is the increase of the error related to the DALE effect.

Another limitation inherent to the reconstruction technique that we identified in this work arises when the viewpoints are approximately 180° from each other. In this case, the camera rays from the two viewpoints become almost parallel to each other and are unlikely to cross. This happened in the analysis of two particular events (i.e., CMEs associated to the MC observed on 2010 December 28 and 2011 February 4), which

exhibited very high error in the triangulation and therefore the results had to be discarded.

5. Summary and Conclusions

We have devised a new methodology (CORSET3D) to estimate CME speed and direction using simultaneous observation from coronagraphs located at two vantage locations. The technique takes advantage of a state-of-the-art supervised computer vision algorithm (CORSET) for the detection and tracking of the plane-of-sky CME projection in the coronagraph FOV, and a stereoscopy methodology for the 3D reconstruction based on epipolar geometry using triangulation and tie-pointing analysis.

The 3D kinematical characterization of the CME events derived with CORSET3D do not depend on visual inspection of the CME features for tie-pointing identification. Hence, the methodology allows 3D reconstruction of the time evolution of the whole CME leading edge in an objective way. As such, CORSET3D is more objective than Sunloop alone, while eliminating a very time-consuming process.

CORSET3D also provides information about both the latitudinal and the longitudinal distribution of the CME front, unlike other methods that provide only the information in longitude. In this work, we have calculated the instantaneous and average radial speeds of a set of CMEs associated with MCs at Earth, as measured at any portion of their leading fronts. In contrast to forward-fitting methodologies (such as the GCS model), we reconstructed the CME front without any geometrical constraint and/or imposed symmetry. Möstl et al. (2014) showed that estimations of the CME arrival time at Earth are dramatically affected by assumptions of idealized fronts.

In this work, we have used observations from the COR2 coronagraphs onboard the twin *STEREO* spacecraft to analyze a set of 20 CMEs directed approximately toward the Earth, which were considered the most likely solar counterpart of MCs observed at Earth between 2008 and 2011. The CME segmentation by CORSET failed in one event, and two other events had to be discarded due to triangulation problems when the separation angle between the two spacecraft was very close to 180°. In the remaining 17 cases, CORSET3D was able to determine some 3D kinematical and morphological parameters such as the average velocity vector (magnitude and direction of propagation), and angular span.

We compared the results derived by CORSET3D with previous works using different methodologies whenever a previous reference related to that event was found. All events from 2008, 2009 and 2010 were compared as well as some observed in 2011, comprising approximately 60% of the events. For four CMEs, there is a significant difference (>10°) in the longitude and in only one case in latitude. When comparing the magnitude of the velocity vector, three events have discrepancies. We realized that, as seen in the coronagraph FOV, most of these events appear superposed in the line of sight by other CMEs. In some cases, there are previous CMEs on the COR2 FOV that may prevent a proper boundary identification by CORSET or may include inaccuracies in the GCS analysis performed in a previous study.

The results from CORSET3D, especially the radial speed distribution and the direction of propagation, are expected to be used as input to future studies of CME geo-effectiveness and arrival times. We also intend to extend the applications of CORSET3D to the Heliospheric Imagers so that we can better understand the propagation of the CME at further distances from the Sun than observed by the coronagraphs.

C.R.B. acknowledges grants #2014/24711-6, #2013/02712-8 and #2012/05436-9 from São Paulo Research Foundation (FAPESP). A.D.L. acknowledges CNPq for grant 304209/2014-7. E.E. acknowledges CNPq for grant 302583/2015-7. Thanks to CAPES for supporting the Graduate Program in Space Geophysics at INPE. R.R.S.d.M. acknowledges São Paulo Research Foundation (FAPESP) for grants #2012/20594-0 and #2013/03530-0, and CNPq for grant 152050/2016-7. The work of G.S. was supported by NASA contract S-13631-Y to NRL.

The Large Angle Spectrometric Coronagraph instrument (LASCO) was constructed by a consortium consisting of the Naval Research Laboratory (Washington DC, USA), the Max Planck Institute for Solar System Research (currently in Gottingen, Germany, formerly known as the Max Planck Institute for Aeronomie in Kathenburg, Lindau, Germany), the Laboratoire d'Astronomie Spatiale (Marseille, France), and the Space Research Group at the University of Birmingham (Birmingham, UK). LASCO is one of a complement of instruments on the *Solar Heliospheric Observatory* satellite (*SOHO*) built in an international collaboration between the European Space Agency (ESA) and National Aeronautics and Space Administration (NASA).

The Sun Earth Connection Coronal and Heliospheric Investigation (SECCHI) was produced by an international consortium of the Naval Research Laboratory (USA), Lockheed Martin Solar and Astrophysics Lab (USA), NASA Goddard Space Flight Center (USA), Rutherford Appleton Laboratory (UK), University of Birmingham (UK), Max Planck Institute for Solar System Research (Germany), Centre Spatiale de Liége (Belgium), Institut d'Optique Theorique et Appliquée (France), and Institut d' Astrophysique Spatiale (France).

References

Billings, D. E. 1966, A Guide to the Solar Corona (New York: Academic)
Bonte, K., Jabobs, C., Robbrecht, E., et al. 2011, SoPh, 270, 253
Boursier, Y., Lamy, P., Llebaria, A., et al. 2009, SoPh, 257, 125
Boursier, Y., Llebaria, A., Goudail, F., et al. 2005, Proc. SPIE, 5901, 13
Braga, C. R. 2015, Study of Coronal Mass Ejections and Their Corresponding Interplanetary Structures Using Combined Observations of Cosmic Ray Detectors and Coronagraphs (São José dos Campos, SP: Instituto Nacional de Pesquisas Espaciais)
Braga, C. R., Stenborg, G., & Dal Lago, A. 2013, AdSpR, 51, 1949
Brueckner, G. E., Howard, R. A., Koomen, M. J., et al. 1995, SoPh, 162, 357
Byrne, J. P. 2015, JSWSC, 5, A19
Byrne, J. P., Maloney, S. A., McAteer, J. R. T., et al. 2010, NatCo, 1, 74
Byrne, J. P., Morgan, H., & Habbal, S. R. 2012, ApJ, 752, 145
Colaninno, R. C. 2012, arXiv:1206.4290
Colaninno, R. C., Vourlidas, A., & Wu, C. C. 2013, JGRA, 118, 6866
Dal Lago, A., Gonzalez, W. D., De Lucas, A., et al. 2013, AdSpR, 51, 1942
Dal Lago, A., Schwenn, R., & Gonzalez, W. D. 2003, AdSpR, 32, 2637
Davies, J. A., Harrison, R. A., Perry, C. H., et al. 2012, ApJ, 750, 23
Domingo, V., Fleck, B., & Poland, A. I. 1995, SoPh, 162, 1
Feng, L., Inhester, B., & Wei, Y. 2012, ApJ, 751, 18
Floyd, O., Lamy, P., Boursier, Y., et al. 2013, SoPh, 288, 269
Gonzalez, W. D., Tsurutani, B. T., & Clúa de Gonzalez, A. L. 1999, SSRv, 88, 529
Gopalswamy, N., Lara, A., Lepping, R. P., et al. 2000, GeoRL, 27, 145
Gopalswany, N., Lara, A., Yashiro, S., et al. 2001, JGRA, 106, 29207
Gopalswamy, N., Yashiro, S., & Akiyama, S. 2007, JGRA, 112, 6112
Gopalswamy, N., Yashiro, S., Michalek, G., et al. 2009, EM&P, 104, 295
Gopalswamy, N., Yashiro, S., Xie, H., et al. 2015, JGRA, 120, 9221

Gosling, J. T. 1990, in Physics of Magnetic Flux Ropes, ed. C. T. Russell, E. R. Priest, & L. C. Lee (Washington, DC: American Geophysical Union), 343
Gosling, J. T., Hildner, E., MacQueen, R. M., et al. 1974, JGR, 79, 4581
Goussies, N., Stenborg, G., Vourlidas, A., & Howard, R. 2010, SoPh, 262, 481
Hapgood, M. A. 1992, P&SS, 40, 711
Haralick, R. L., Shanmugam, D., & Dinstein, I. 1973, ITSMC, 3, 6
Howard, R. A., Brueckner, G. E., St Cyr, O. C., et al. 1997, in Coronal Mass Ejections, ed. N. Crooker, J. A. Joselyn, & J. Feynman (Washington, DC: American Geophysical Union), 17
Howard, R. A., Moses, J. D., Vourlidas, A., Newmark, J. S., et al. 2008, SSRv, 136, 67
Howard, R. A., Sheeley, N. R., Jr., Michels, D. J., & Koomen, M. J. 1985, JGR, 90, 8173
Howard, T. A., & DeForest, C. E. 2014, ApJ, 796, 33
Hutton, J., & Morgan, H. 2017, A&A, 588, A68
Inhester, B. 2006, arXiv:astro-ph/0612649
Kaiser, M. L., Kucera, T. A., Davila, J. M., et al. 2008, SSRv, 136, 5
Liewer, P. C., De Jong, E. M., Hall, J. R., et al. 2009, SoPh, 256, 57
Liewer, P. C., Hall, J. R., Howard, R. A., et al. 2011, JASTP, 73, 1173
Liewer, P. C., Panasenco, O., Vourlidas, A., et al. 2015, SoPh, 290, 3343
Liu, Y., Davies, J. A., Luhmann, J. G., et al. 2010, ApJL, 710, L82
Liu, Y., Luhmann, J. G., Bale, S. D., & Lin, R. P. 2011, ApJ, 734, 84
Liu, Y. D., Luhmann, J. G., Möstl, C., et al. 2012, ApJL, 746, 15
Lugaz, N. 2010, SoPh, 267, 411
Lugaz, N., Farrugia, C. J., Davies, J. A., et al. 2012, ApJ, 759, 68
Lugaz, N., Vourlidas, A., & Roussev, I. I. 2009, AnGeo, 27, 3479
Mierla, M., Davila, J., Thompson, W., et al. 2008, SoPh, 252, 385
Mierla, M., Inhester, B., Antunes, A., et al. 2010, AnGeo, 28, 203
Mierla, M., Inhester, B., Marqué, C., et al. 2009, SoPh, 259, 123
Moran, T. G., & Davila, T. M. 2004, Sci, 305, 66
Moran, T. G., Davila, T. M., & Thompson, W. T. 2010, ApJ, 712, 453
Morgan, H., Byrne, J. P., & Habbal, S. R. 2012, ApJ, 752, 144
Möstl, C., Amla, K., Hall, J. R., et al. 2014, ApJ, 787, 119
Möstl, C., Rollett, T., Lugaz, N., et al. 2011, ApJ, 741, 34
Olmedo, O., Zhang, J., Wechsler, H., et al. 2008, SoPh, 248, 485
Owens, M., & Cargill, P. 2004, AnGeo, 22, 661
Richardson, I. G., & Cane, H. V. 2010, SoPh, 264, 189
Robbrecht, E., & Berghmans, D. 2004, A&A, 425, 1097
Robbrecht, E., Patsourakos, S., & Vourlidas, A. 2009, ApJ, 701, 283
Rollett, T., Möstl, C., Temmer, M., et al. 2012, SoPh, 276, 293
Rouillard, A. P., Davies, J. A., Forsyth, R. J., et al. 2008, GeoRL, 35, 10110
Savani, N. P., Owens, M. J., Rouillard, A. P., Forsyth, R. J., & Davies, J. A. 2010, ApJL, 714, L128
Schwenn, R., Dal Lago, A., Huttenen, E., & Gonzalez, W. D. 2005, AnGeo, 23, 1033
Sheeley, N. R., Walters, J. H., Wang, Y. M., & Howard, R. A. 1999, JGRA, 104, 24739
Shen, C., Wang, Y., Pan, Z., et al. 2014, JGRA, 119, 5107
St Cyr, O. C., Howard, R. A., & Sheeley, N. R., Jr 2000, JGRA, 105, 18169
Temmer, M., Vrsnak, B., Rollett, T., et al. 2012, ApJ, 749, 57
Thernisien, A. F. R. 2011a, ApjS, 194, 33
Thernisien, A. F. R., Howard, R. A., & Vourlidas, A. 2006, ApJ, 652, 763
Thernisien, A. F. R., Vourlidas, A., & Howard, R. A. 2009, SoPh, 256, 111
Thernisien, A. F. R., Vourlidas, A., & Howard, R. A. 2011b, JASTP, 73, 1156
Thompson, W. T. 2006, A&A, 449, 791
Tousey, R., Rycroft, M. J., & Runcorn, S. K. (ed.) 1973, Space Research XIII (Berlin: Akademie)
Vourlidas, A., Balmaceda, L., Stenborg, G., & Dal Lago, A. 2017, ApJ, 838, 141
Vourlidas, A., Lynch, B. J., Howard, R. A., & Li, Y. 2013, SoPh, 284, 179
Wang, Y.-M., & Colaninno, R. 2014, ApJL, 784, L27
Webb, D. F., & Howard, R. A. 1994, JGR, 99, 4201
Webb, D. F., & Howard, T. A. 2012, LRSP, 9, 3
Wood, B. E., Howard, R. A., Plunkett, S. P., et al. 2009, ApJ, 694, 707
Yashiro, S., Gopalswamy, N., Michalek, G., et al. 2004, JGRA, 109, A07105
Yashiro, S., Michalek, G., & Gopalswamy, N. 2008, AnGeo, 26, 3303